Spring 5-2016

Bending Loss Mitigation by Surface Plasmon Resonance

Daniel Steven Spoor
Rose-Hulman Institute of Technology

Bending Loss Mitigation by Surface Plasmon Resonance

A Thesis

Submitted to the Faculty

of

Rose-Hulman Institute of Technology

by

Daniel Steven Spoor

In Partial Fulfillment of the Requirements for the Degree

of

Master of Science in Optical Engineering

May 2016

ROSE-HULMAN INSTITUTE OF TECHNOLOGY

Final Examination Report

Daniel S. Spoor	Optical Engineering
Name	Graduate Major

Thesis Title: Bending Loss Mitigation by Surface Plasmon Resonance

DATE OF EXAM: June 12, 2016

EXAMINATION COMMITTEE:

	Thesis Advisory Committee	Department
Thesis Advisor:	Azad Siahmakoun	PHOE
	Sergio Granieri	PHOE
	Daniel Morris	CHEM

PASSED X **FAILED** _____

Abstract

Spoor, Daniel Steven

M.S.O.E

Rose-Hulman Institute of Technology

May 2016

Bending Loss Mitigation by Surface Plasmon Resonance

Thesis Advisor: Dr. Azad Siahmakoun

Surface plasmon resonance can be used to confine a wave within a thin metal film. The resultant wave is very well-confined by the extreme refractive index difference between the metal and the ambient medium. Such confinement can be used to guide waves under extreme conditions such as subwavelength channels or through extremely tight bends where radiation losses would normally dissipate the wave.

A nichrome thin film was deposited and etched as a shadow alongside a series of multi-mode SU-8 slab waveguides with extremely sharp angled bends. Light from a Helium-Neon laser was coupled into these waveguides and the power transmitted was measured and compared to a sample without a nichrome thin film. A total attenuation of signal was found in the non-metallic sample, while a steady signal was successfully transmitted through the sample with the thin film.

Dedication

I prepared explosive runes this morning.

Acknowledgments

I would like to thank my advisor, Dr. Azad Siahmakoun, for teaching me everything I know about research methodology, and for his patience when I was not exactly the quickest study. After all his tutelage, life can only get easier from here. Interpret that as you will.

I would also like to thank Dr. Richard Liptak for his assistance. He always made himself available whenever I needed help troubleshooting a process, which was quite often. His bleak humor also made the year I spent on fabrication a little less bleak.

Similarly, I would like to thank Brian Fair for the long hours he spent with me in the clean room. On some days, his was the only human face I would see. Well, the top half of it anyway.

Finally, I wish to thank my parents for their unwavering and frequently fanatical support.

Table of Contents

Contents

List of Figures

Figures Page

List of Tables

Table Page

List of Abbreviations

CMOS	Complementary Metal-Oxide-Semiconductor
HeNe	Helium-Neon Laser
NA	Numerical Aperture
SEM	Scanning Electron Microscope/Microscopy
SPP	Surface Plasmon Polariton
SPR	Surface Plasmon Resonance
TE	Transverse Electric (Wave)
TM	Transverse Magnetic (Wave)
UV	Ultraviolet
WEC	Wedge Error Compensation

List of Symbols

Greek Characters

α	Attenuation Coefficient
β	Propagation Constant
Γ	Loss (Electron Harmonics)
Δ	Phase Shift
ε	Permittivity
ε_r	Relative Permittivity
θ_c	Critical Angle
θ_m	Angle of Guided Mode
λ	Wavelength
λ_m	Wavelength of a Given Mode
η	Loss (Optical Coupling)
ρ	Complex Refractance
Ψ	Amplitude Ratio
ω	Angular Frequency
ω_0	Resonant Frequency
ω_p	Plasmon Frequency

Latin Characters

$\bar{E}$	Electric Field
i	Imaginary Number
k	Wave Number

$\bar{k}$	Wave Vector
m	Mode Number
n	Index of Refraction
ñ	Complex Index of Refraction
q	Charge of an Electron
R_p	Reflectivity (P-Polarization)
R_s	Reflectivity (S-Polarization)
Z_c	Spatial Coherence Length

1. Introduction

1.1 History and Overview

Since the development of low-loss optical fibers in the early 1970s and the subsequent creation of limited fiber telephone networks, optical components and devices have become increasingly important in nearly every field of computing and networking. The demand for greater bandwidth and shorter delays has led to the development and adoption of vast fiber optical networks, including such massive undertakings as the 28,000 km Fiber-Optic Link Across the Globe.

It then comes as no surprise that this interest in fiber networking has led to an industry-wide push to incorporate new optical components into existing technologies and even create all-optical devices to replace modern electrical products. High potential bandwidth and incredibly fast switching speeds have made all-optical processors and converters an appealing candidate for future substitution and eventual replacement for their current all-electrical counterparts.

As a technology in its infancy, all-optical components face a number of serious challenges before they can be widely adopted. Chief among them is the development of micro- and nanometer-scale optical components. Unlike electrical signals which ride predominantly on the outer surface (skin) of their conductors, optical waves have a tendency to “leak” from their confines, dissipating power and potentially interfering with nearby channels. This effect is particularly noticeable in nanometer-scale devices. The very means by which optical waves

propagate through materials makes them difficult to contain on such a small scale.

Numerous techniques are being developed to mitigate or completely counteract this tendency. Chief among these is the use of surface plasmon resonance (SPR) to control and contain optical waves. SPR devices rely on thin metal or graphene films and their unique interaction with electromagnetic radiation to confine a wave to an exceedingly small area, usually at the cost of large propagation losses. Even with this large attenuation, devices based on plasmonic films hold great promise in extremely small devices such as microprocessors.

One of the potential applications of plasmonic films is the creation of metallic surface-mounted waveguides (SMW). These structures consist of an extremely thin layer of metal deposited on a substrate and etched into the desired shape. In this way, they resemble their more conventional glass and polymer counterparts, albeit with some very significant differences in functionality. Over sufficiently short distances, metallic films are transparent enough to transmit some specific frequencies of light. As a general rule of thumb, such devices are limited to distances of one hundred or so microns, though devices as long as 1mm have been constructed. Longer devices can be constructed, but become much more difficult to simulate and require impractically high powers to counteract the enormous propagation losses.

These devices are capable of entirely sequestering the propagating wave to an incredibly narrow channel, as thin as a few nanometers. These contained waves are almost entirely isolated from nearby structures, preventing interference with other devices and limiting cross-talk. This enables waveguides to be placed orders of magnitude closer together than glass or polymer

SMW of similar dimensions. Such devices are likely to be considered for use in many optical devices in the future.

In addition to being able to carry optical signals, plasmonic films are capable of entirely reflecting or absorbing specific wavelengths of light. In this way, a thin coating of metal can be used to reflect a leaking signal back into its waveguide, depending on material, construction, and wavelength. A totally enveloping coating of the right specifications is capable of containing the signal within the coated waveguide. The reflective properties of metallic films are integral to this thesis and shall be discussed at great length.

Plasmonic films may also be subject to optical coupling. A signal may move freely between a plasmonic waveguide and a more conventional glass or polymer one (or even another metal strip), so long as they are exceedingly close (physical contact may be required) and the proper conditions are met. This allows for the creation of a number of novel apparatuses, some of which will be explored later on. Such a construction also allows for an optical wave to travel through a plasmonic strip alongside another waveguide. In this way, a portion of the signal may be allowed to “skip” a section of waveguide, should the loss through that section be too high. This concept forms the basis of this research.

1.2 Motivations of Research

Attenuation of an optical signal is one of the greatest considerations when designing a device. High attenuation can destroy a signal, reducing its power so greatly that it is no longer meaningfully distinguishable from noise or modulation artifacts. As such, it is generally ideal to create a system with as little loss as possible so as to ensure the greatest signal quality.

In larger devices, this can be accomplished by introducing a gain to offset the loss, usually in the form of a solid-state amplifier like an erbium-doped fiber amplifier (EDFA). This is how all fiber networks are built, with numerous repeater stations amplifying the signal at regular intervals. However, in micro- and nanometer-scale devices, this is impossible, as the amplifier would need to be larger than the entire device to provide sufficient gain. As such, the only recourse is to limit the various sources of loss as much as possible. Unfortunately, geometry or other design specifications may introduce excessive and unavoidable loss. Exceptionally tight turns, hard angles, and inclusions in the waveguide may even entirely attenuate the signal. In these cases, it may be advantageous to entirely eliminate such structures. This can be achieved through the use of thing metal films.

When the loss caused by a sharp turn, breakage, or dramatic taper (collectively referred to as geometric losses) becomes so great as to almost entirely attenuate the signal, even the high loss of a plasmonic waveguide becomes a much-preferred alternative. A metallic strip placed in contact with a conventional waveguide will always carry a small portion of that signal alongside the primary waveguide. In this way, even if the signal within the primary waveguide is entirely

lost, it may be restored, albeit at much lower power, when the nearby signal couples or reflects back in. In this way, nearly any flaw in the primary waveguide, from fabrication errors to unreasonably sharp turns may be compensated for.

The objective of this research was to create a device and experimental regime by which the efficacy of using plasmonic coupling and reflection to mitigate geometrical losses can be determined. To ensure the validity of the results, a device was created such that geometrical losses would be so great as to render the signal irrecoverable by any available detector. In this way, any signal safely transmitted and recovered would owe its existence entirely to plasmonic interactions.

1.3 Literature Review

Confinement of a guided wave by plasmonic surfaces can be achieved with a number of arrangements. One such arrangement is the plasmonic slot waveguide. Slot waveguides are devices wherein light is guided in a dielectric with low refractive index (often air) between two slabs of some material with much higher index. Conventional slot waveguides often consist of silicon slabs and an air-filled slot. These devices are capable of subwavelength confinement of light but can be improved considerably through the use of metal films.

Yang, et al designed, modeled and fabricated a slot-to-slot coupler linking a silicon slot waveguide with a gold film slot waveguide. A slot waveguide consisting of an air-filled slot and surrounding silicon slabs guided light into a plasmonic slot consisting of a 20nm gold film laid

isotropically over the slabs. An 80nm slot was created and used to carry 1550nm IR light. The extremely large refractive index of gold (n=-96+11i) provides excellent containment relative to silicon slot waveguides. Their results indicate a considerably greater confinement within this configuration [1].

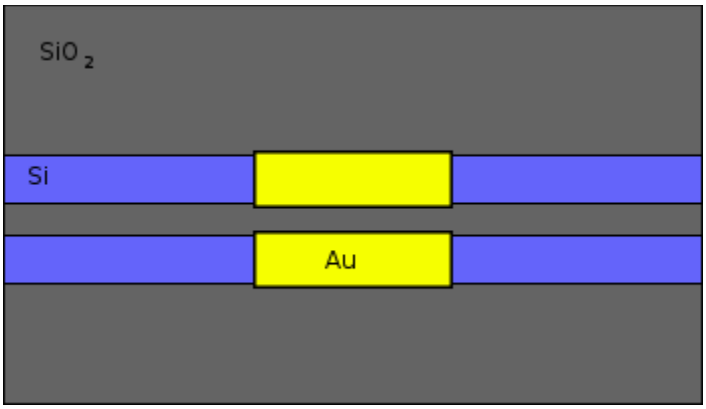

Figure 1.1 Gold Film on Silicon Plasmonic Slot Waveguide

Figure 1.1 shows an arrangement similar to Yang, et al [2]. Two slabs of silicon are fabricated atop silicon dioxide. Light can be contained within the air-filled slot between the slabs, even if the width of the slot is significantly smaller than the wavelength of the light. Metal film deposited on all sides of a slot waveguide creates a plasmonic slot waveguide, here shown with a gold film. The enormous real refractive index of metal films provides exceptional confinement in slot waveguides.

Other groups have demonstrated that similarly constructed slot waveguides may limit losses in exceptionally tight bends. Veronis et al simulated a plasmonic slot waveguide with 50nm and 100nm air slot surrounded by thin silver slabs. A finite-difference frequency domain study was conducted to determine the transmission of light through right-angle bends as in

Figure 1.2. It was found that the transmission increased with wavelength. This is due to the greater confinement granted by a higher permittivity in the metal as the frequency decreases [3].

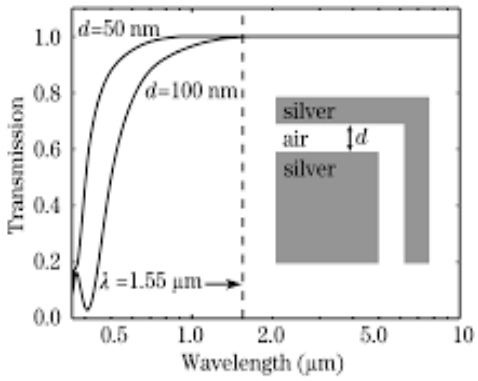

Figure 1.2 Transmission Characteristics of a Right-Angle Bend through a Simulated Plasmonic Slot Waveguide [3]

Veronis et al simulate a hard-angle bend in a plasmonic slot waveguide, shown in Figure 1.2. The inset graph shows the transmission of the structure with respect to wavelength through the IR region. A clear and dramatic increase in transmission occurs with increase in wavelength due to increasing permittivity in the silver film. The inset shows the structure simulated, depicted from above [3].

Not all plasmonic waveguides are constructed from slot waveguides. Krasavin and Zayats proposed a dielectric ridge waveguide constructed on a metal film. In this arrangement, a silicon slab is placed atop a metal film directly. Silicon ridge waveguides placed atop silicon dioxide are common in subwavelength confinement but tend to suffer losses as radiation seeps into the substrate.

Krasavin and Zayats designed a CMOS-compatible arrangement using aluminum or gold as the metal film and simulated the dispersion of the waveguide. Since a high dispersion necessarily results in poor confinement, it is an exceptionally important quantity in determining the effectiveness of subwavelength waveguides. The study concluded that the presence of metal films greatly decreases the dispersion, particularly as the wave number increased [3].

A similar construction was presented by Sefunc et al. Their device consists of an SU-8 waveguide atop a thin silicon dioxide buffer deposited over a gold film. The waveguide was designed to be 2μm square and the oxide and metal films both 100nm. A simulation was performed replicating a smooth-bent waveguide of narrow (variable) radius carrying 1.55μm light. The intention was to investigate the use of this construction to mitigate geometric losses resulting from narrow bends [4].

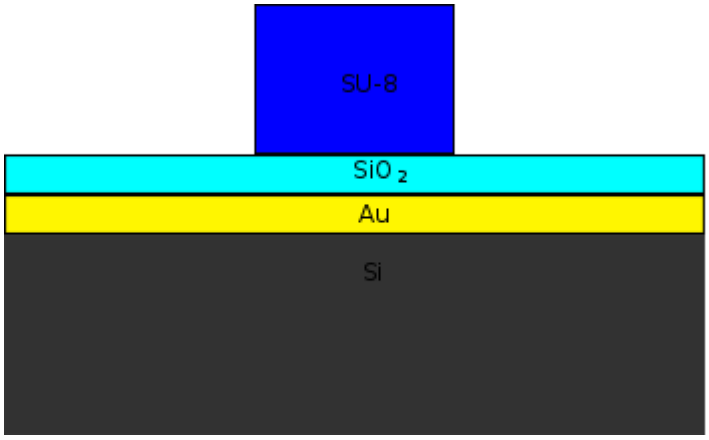

Figure 1.3 Gold Film-Aided Confinement in SU-8 Waveguide

Figure 1.3 shows an arrangement similar to that used by Sefunc et al [4]. They simulated

a gold strip atop a silicon substrate. The SU-8 waveguide is insulated from the gold by a thin layer of silicon dioxide. This buffer layer provides a lower-index layer necessary for the excitation of surface plasmons in the gold film.

The study used a finite difference model to directly compare the experimental and control waveguides. One set of data presents power distributions in the waveguides during bending, qualitatively contrasting their shape. This data presents radically different power distributions inside and outside the waveguide. Notably, the metal underneath the waveguide prevented leakage into the substrate, while the metal alongside the waveguide prevented outwards radiation pointing to the substrate [4].

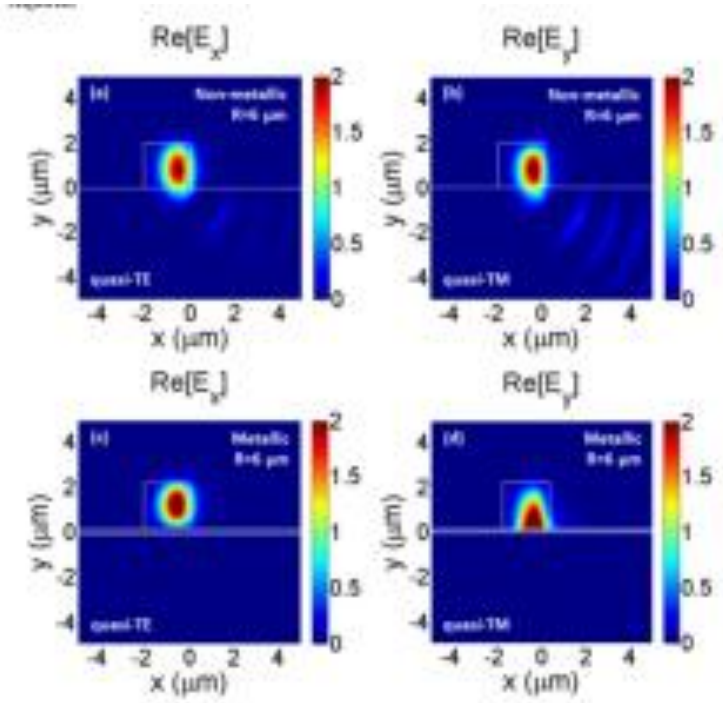

Figure 1.4 Simulated Electric Field in Gold Film-Aided Bent SU-8 Waveguide [4]

Sefunc et al demonstrate the difference between plasmonic and non-plasmonic waveguides as they meet harsh turns. Figure 1.4 depicts the real component of the electric field in the x and y directions as they undergo a 6μm turn. The top diagrams show the profile of the control sample, while the lower diagrams show the profile of the plasmonic sample. It is immediately visible that in the plasmonic samples, the electric field does not penetrate the substrate underneath the waveguide. The control sample also shows a number of ripples below and to the right of the waveguide. These ripples represent the light radiating outwards due to the turn. These ripples are noticeably absent in the sample with the metal film. This is due to confinement by the metal just outside the waveguide. This mode trapped by the metal film is visible in the bottom right image as a small concentration of electric field at the three-layer boundary [4].

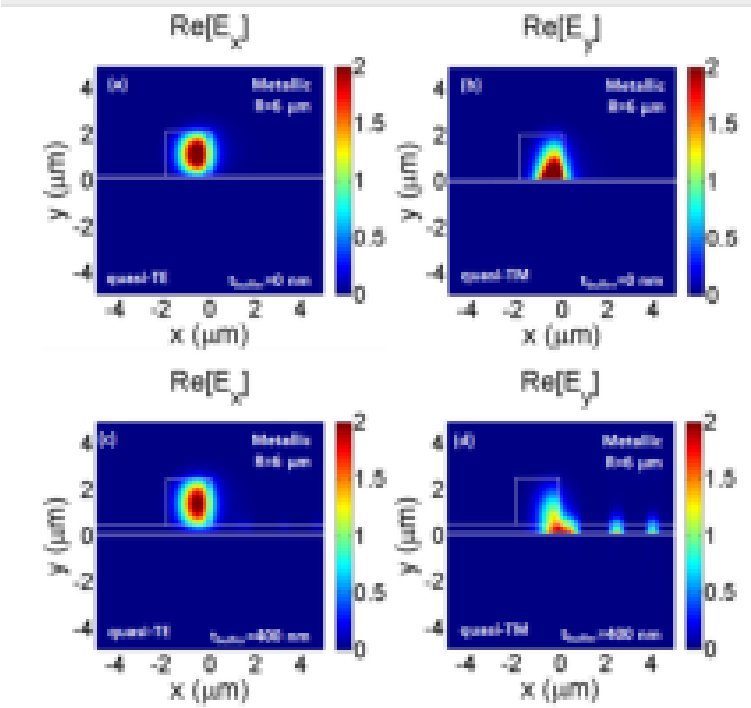

Figure 1.5 The Effects of Buffer Layer on Gold Film-Aided Bent SU-8 Waveguide [4]

In Figure 1.5, Sefunc et al allowed the thickness of the buffer oxide layer between the waveguide and the metal to vary. The top images show the real component of the electric field when there is no buffer layer, while the lower shows the result if the buffer layer is 400nm. The interesting result of this study is the leakage of the y-component of the electric field into the metal when the buffer layer is 400nm. The majority of the field (and therefore power) is concentrated fully outside the waveguide, with pockets of considerable power located far outside the waveguide. These pockets likely represent radiation losses caused by turning [4].

Another set of data simulates the loss directly, estimating the loss for both TE and TM waves as they undergo sharp turns (see Figure 1.6). Here the radius was allowed to vary, showing the relationship between loss and the radius of the turn. A substantially lower loss was observed when the metal layer was added.

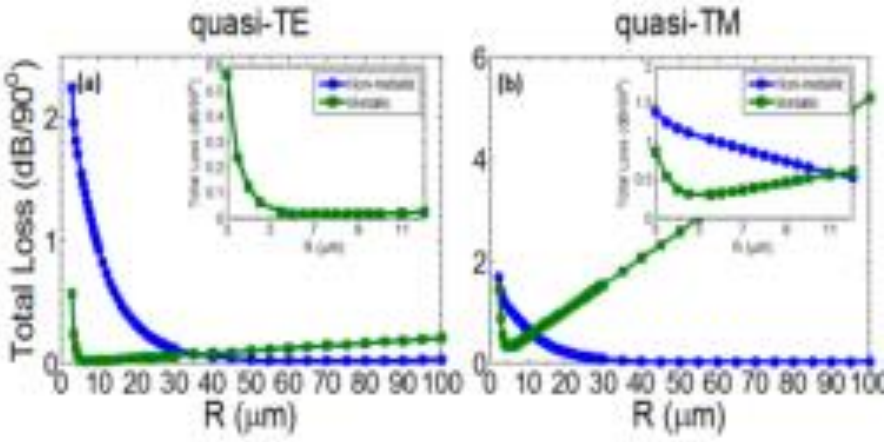

Figure 1.6 Simulated Loss Characteristics of Gold Film-Aided Bent SU-8 Waveguide [4]

Figure 1.6 shows the loss, reported in dB per quarter turn of a round bend, with respect to the radius of the bend. The buffer layer here is again 100nm. In the non-metallic control, the loss decreases exponentially as the radius increases, regardless of orientation of the wave.

However, the metallic samples show a strong dependence on polarization. In the TE case, the loss starts considerably lower than the control, dropping near zero at around 6μm of radius. However, above this point, the loss starts to increase, eventually becoming greater than that of the non-metallic sample at about 35μm. This increase in loss is due to the absorption of the metal film. While the bend was tight, the metal assists in confining the guided wave. As the radius increases, the radiation losses due to turning decrease and the guided wave sinks into the metal, which has a vastly higher attenuation than the waveguide. In the TM instance, there is little positive interaction with the metal. This is because the TM orientation is incapable of exciting surface plasmon resonance. The loss increases sharply for the metallic sample in this regime, again caused by absorption in the metal. Without any plasmonic activity, the metal simply acts as a bulk metal, absorbing the light with an incredibly high attenuation [4].

2. Theory of Light Propagation in Waveguides

2.1 Guided Wave Optics

To develop a theory of a guided wave, it is useful to start at the simplest possible model. Consider a transverse wave (TE) bouncing between a pair of perfect mirrors with an arbitrary angle θ between the wave and the wall of the mirror. This wave propagates in two directions, the longitudinal z-axis and the transverse y-axis. Reflections alternate at angles θ and -θ on each surface. Upon reflection, a phase shift of π is observed.

In order for the ray to propagate smoothly, it is necessary to consider only those waves that reproduce themselves at every other reflection (those for which θ is constant for all reflections). Such waves are referred to as modes. Modes, then, by their very nature are discrete conditions of reflection. Modes may only exist then when the above conditions are satisfied, leading to the relation

$$sin(\theta_m) = m\frac{\lambda}{2d} \tag{2.1}$$

where d is the distance between mirrors and m an integer representing a valid mode.

It is now possible to define a wave vector in terms of the available modes. A wave vector, by definition, represents the direction and wavelength of the wave and can be defined as

$$k_y = \frac{2\pi}{\lambda} sin\theta \tag{2.2}$$

and can then be rewritten in terms of (2.1), giving

$$k_y = m\frac{\pi}{d} \tag{2.3}$$

This wave vector quantifies the propagation of the wave in the y-axis, toward and away from the mirrors. Naturally, this wave is also moving in the z-axis. The wave vector in this direction is similarly

$$k_z = \frac{2\pi}{\lambda} cos\theta \tag{2.4}$$

This term is also known as the propagation constant, represented as β. Applying trigonometric identities, the conventional form is written

$$\beta_m^2 = \left(\frac{2\pi}{\lambda}\right)^2 - \frac{m^2\pi^2}{d^2} \tag{2.5}$$

At this point, it is possible to do away with the mirrors and consider a wave traveling through a planar waveguide. In this waveguide, a material of high refractive index is sandwiched between two areas of identical, lower refractive index. The wave is still traveling in the z direction. Now that it is no longer possible to rely on the assumption that the phase difference upon reflection is exactly π, it is necessary to rewrite (2.1) to establish the mode conditions in terms of the phase difference φ.

$$\frac{2\pi}{\lambda} 2dsin\theta - 2\phi = 2\pi m \tag{2.6}$$

Now, the phase difference upon reflection depends on the polarization of the incident wave. The phase shift upon reflection of a TE wave is

$$tan\frac{\phi}{2} = \sqrt{\frac{cos^2\theta_c}{cos^2\theta} - 1} \tag{2.7}$$

where θ_c is the critical angle. Substituting this into (2.6), the self-consistency condition for TE polarized modes is obtained.

$$tan\left(\pi\frac{d}{\lambda}sin\theta - m\frac{\pi}{2}\right) = \sqrt{\frac{cos^2\theta_c}{cos^2\theta} - 1} \tag{2.8}$$

Likewise, the phase shift for a TM-polarized wave is

$$tan\left(\pi\frac{d}{\lambda}sin\theta - m\frac{\pi}{2}\right) = \sqrt{\frac{cos^2\theta_c}{cos^2\theta} - 1} \tag{2.9}$$

leading to a self-consistency condition for the TM wave of

$$tan\left(\pi\frac{d}{\lambda}sin\theta - m\frac{\pi}{2}\right) = \frac{-1}{sin^2\theta}\sqrt{\frac{cos^2\theta_c}{cos^2\theta} - 1} \tag{2.10}$$

Any wave which is capable of satisfying the appropriate self-consistency condition will propagate through this waveguide [5].

It is often useful to consider the effective refractive index of a propagating mode. Consider a waveguide of width 100μm and n=1.595, clad by air (n=1.000). These conditions are very similar to those faced by a TE wave in the waveguides fabricated and described in Chapter 3. For this configuration, the critical angle θ_c=0.9848rad (56.42deg). With this, it is possible to find the angle of propagation corresponding to each mode. Each propagation angle is unique, the product of this propagation angle and the index of refraction for the TE0 mode gives the effective refractive index of the mode.

Table 2.1 Estimated Refractive Index of TE Modes

Mode number (m)	Effective Refractive Index n_{eff}
1	1.5942
10	1.5867
20	1.5783
50	1.5533
100	1.5115

It is now possible to examine how waves propagate within this waveguide, rather than just which waves can. To do this, it helps to start with an alternate definition of a mode, defining it as a solution to Maxwell's propagation equation.

$$\nabla^2 \bar{E}(r) + k^2 n^2 \bar{E} = 0 \qquad (2.11)$$

The electric field in its basic form is expressed as

$$\bar{E}(r,t) = \bar{E}(r)e^{i\omega t} \qquad (2.12)$$

Combining these two equations for waves normally incident on the face of the waveguide gives

$$\left(\frac{\partial^2}{\partial x^2}+\frac{\partial^2}{\partial y^2}\right)\bar{E}(x,y)+(k^2n^2(\bar{r})-\beta^2)\bar{E}(x,y)=0 \qquad (2.13)$$

It is customary at this point to make one dimension of the waveguide semi-infinite, making the derivative of the field zero. This simplifies the math greatly and is not harmful to building an understanding of the nature of wave propagation. This equation can then be simplified to

$$\frac{\partial^2}{\partial x^2}\bar{E}(x,y)+(k^2n^2(\bar{r})-\beta^2)\bar{E}(x,y)=0 \qquad (2.13)$$

This equation holds true for every section of the waveguide, with the wave vector and index of refraction changing appropriately. In the cladding, it is necessary for all derivatives of E to be negative or zero. Otherwise, the field would increase indefinitely outside of the waveguide, resulting in extremely poor confinement. A negative derivative therefore requires that

$$kn_{clad}<\beta \qquad (2.14)$$

The solution to (2.13) of any such modes results in exponential decay in the cladding, a result which makes intuitive sense if the waveguide is to actually guide waves. Similar logic can be used to bound the conditions inside the waveguide. If k_n is greater in the cladding than the core, the wave will naturally begin to propagate within the cladding. As such, it is necessary that

$$kn_{core} > \beta \tag{2.15}$$

With the bounds of each value in place, it is helpful to step back for a moment and consider the geometry of what is going on. The wave vector comprises the path of the light as it propagates through the waveguide. The propagation constant represents the forward (z) motion of the wave. These two vectors can be drawn together to form the basis of a right triangle. This new term h represents the propagation in the direction perpendicular to the propagation constant. As a result of this, it is possible to write

$$\beta^2 + h^2 = k^2 n_2^2 \tag{2.16}$$

This is an important identity helpful for computing the propagation constant.

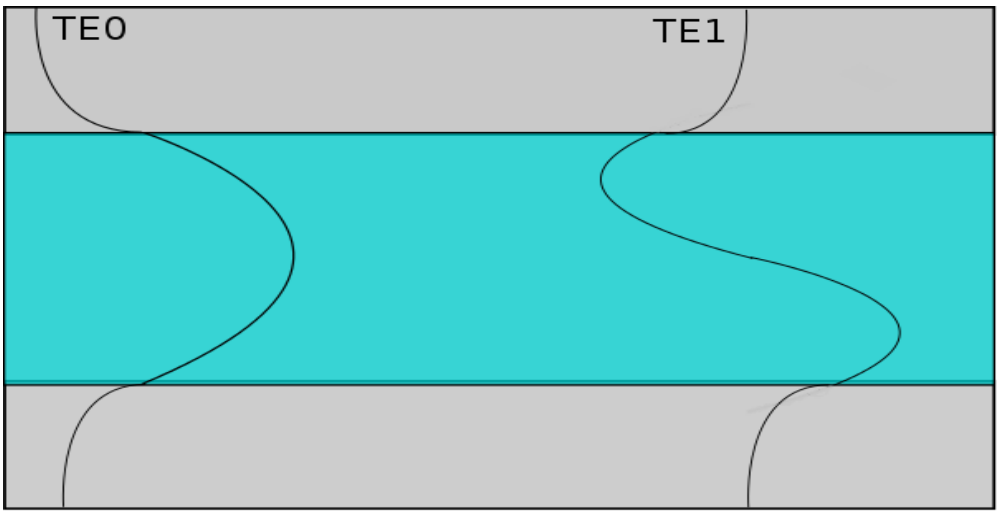

Figure 2.1 TE Mode Distribution in Arbitrary Slab Waveguide

An arbitrary waveguide guides the 0^{th} and 1^{st} transverse electric modes in Figure 2.1. The electric field within the waveguide is sinusoidal with a number of nodes (turning points) based

on the order of the mode. In the cladding, the electric field decays exponentially to zero. A large multi-mode waveguide may carry many hundreds or even thousands of modes.

With the relationship between propagation constant and wave vector established, it is now possible to consider the closed-form solution for the electric field within a waveguide. Any possible solution must satisfy the wave equation

$$\nabla^2 E_y = \frac{n_m^2}{c^2}\frac{\partial^2 E_y}{\partial t^2} \tag{2.17}$$

For the TE mode, the electric field can be expressed as

$$E_y(x,z,t) = \varepsilon_y(x)e^{i(\omega t-\beta z)} \tag{2.18}$$

with

$$\varepsilon = \begin{Bmatrix} Ce^{-qx} & 0 \leqslant x < \infty \\ C\big(cos(hx) - (q/h)sin(hx)\big) & -d \leqslant x \leqslant 0 \\ C\big(cos(hd) + (q/h)e^{p(x+d)}\big) & -\infty < x < -d \end{Bmatrix} \tag{2.19}$$

where C, q, p are arbitrary constants and d is the boundary of the waveguide.

Solving (2.17) with these conditions gives

$$h = (n_2^2k^2 - \beta^2)^{1/2} \tag{2.20a}$$

$$q = (\beta^2 - n_1^2k^2)^{1/2} \tag{2.20b}$$

$$p = (\beta^2 - n_3^2 k^2)^{1/2} \tag{2.20c}$$

The TM mode can be given the same treatment, resulting instead with

$$E_x(x,z,t) = \frac{\beta}{\omega\epsilon} H(x) e^{i(\omega t - \beta z)} \tag{2.21}$$

with

$$H(x) = \begin{Bmatrix} -C[(h/q)cos(ht) + sin(ht)]e^{p(x+t)} & x < -t \\ C[-(h/q)cos(hx) + sin(hx)] & -t < x < 0 \\ -(h/q)Ce^{qx} & x > 0 \end{Bmatrix} \tag{2.22}$$

Unfortunately, solving this is considerably more difficult than it is in the TE case. As such, solutions are pulled from the transcendental equation

$$tan(ht) = \frac{h(p+q)}{h^2 - pq} \tag{2.23}$$

With these equations in place, it is possible to accurately describe both TE and TM waves inside of a waveguide and in its cladding [6].

Of course, these equations only hold for a waveguide confining light in one dimension. Surprisingly many functional devices can be successfully modeled as such due to extreme aspect ratios and a subwavelength dimension on one axis. However, the waveguides discussed herein cannot be reasonably reduced to two dimensions. As such, it is important to know how the

inclusion of an additional dimension impacts the propagation of light.

Unfortunately, a comprehensive description of any but the simplest three-dimensional waveguide is excessively complicated. That being said, it is possible to gain a qualitative understanding of the properties of a three-dimensional waveguide by examining the simple case of a dielectric strip (n_1) of rectangular cross-section surrounded by four regions of refractive index n_2, n_3, n_4, and n_5 such that, n_2, n_3, n_4, $n_5 < n_1$.

The modes of the propagating wave are then separated into two groups, E^x and E^y, based on the plane in which the modes oscillate. These modes are further identified by their order in x and y, denoted by the integers p and q. The modes can then be described as E^x_{pq} and E^y_{pq}. If the index contrast is relatively small, total internal reflection polarizes these waves such that for E^x, E_y and E_z are essentially zero (and the opposite is true for E^y). Because of this, E^x and E^y are more-or-less independent and can be solved for individually.

While no exact solution exists for this problem, there is an approximate solution that accurately describes a low-contrast dielectric slab waveguide. The two modal groups above are described and solved separately in a manner similar to the derivation of the planar slab waveguide. For E^y, the wave vector in the propagating direction can be written as

$$k_z = \sqrt{k_1^2 - \left(\frac{\pi p}{a}\right)^2 \left(1 + \frac{A_3 + A_5}{\pi a}\right)^{-2} - \left(\frac{\pi q}{b}\right)^2 \left(1 + \frac{n_2^2 A_2 + n_4^2 A_4}{\pi a}\right)^{-2}} \qquad (2.24)$$

where

$$A_n = \frac{\pi}{\sqrt{k_1^2 - k_n^2}} \tag{2.25}$$

for n=2, 3, 4, 5, corresponding to the waveguide region and a, b are the dimensions of the core in x and y, respectively [6].

2.2 Waveguide Coupling

Any time light is coupled in or out of a waveguide, some of the power does not make it through the transition. Light may be reflected off of the surface or even just miss the target entirely. First, consider reflected loss. Whenever light moves from one material to another, a Fresnel reflection takes place, and a calculable portion of that light is reflected. This portion differs for the two orientations of linear polarization (s and p) and is written out for each.

$$R_s = \left| \frac{n_1 cos\theta_i - n_2 \sqrt{1 - \left(\frac{n_1}{n_2} sin\theta_i\right)^2}}{n_1 cos\theta_i + n_2 \sqrt{1 - \left(\frac{n_1}{n_2} sin\theta_i\right)^2}} \right|^2 \tag{2.26}$$

$$R_p = \left| \frac{n_1 \sqrt{1 - \left(\frac{n_1}{n_2} sin\theta_i\right)^2} - n_2 cos\theta_i}{n_1 \sqrt{1 - \left(\frac{n_1}{n_2} sin\theta_i\right)^2} + n_2 cos\theta_i} \right|^2 \tag{2.27}$$

Here, n_1 and n_2 are the index of refraction of the first and second materials, respectively. The angle θ_i is the angle of incidence of the light on the second surface. For unpolarized light (used in this experiment), the average of these values is taken. As is immediately obvious, for very small angles, this reflected power goes to zero.

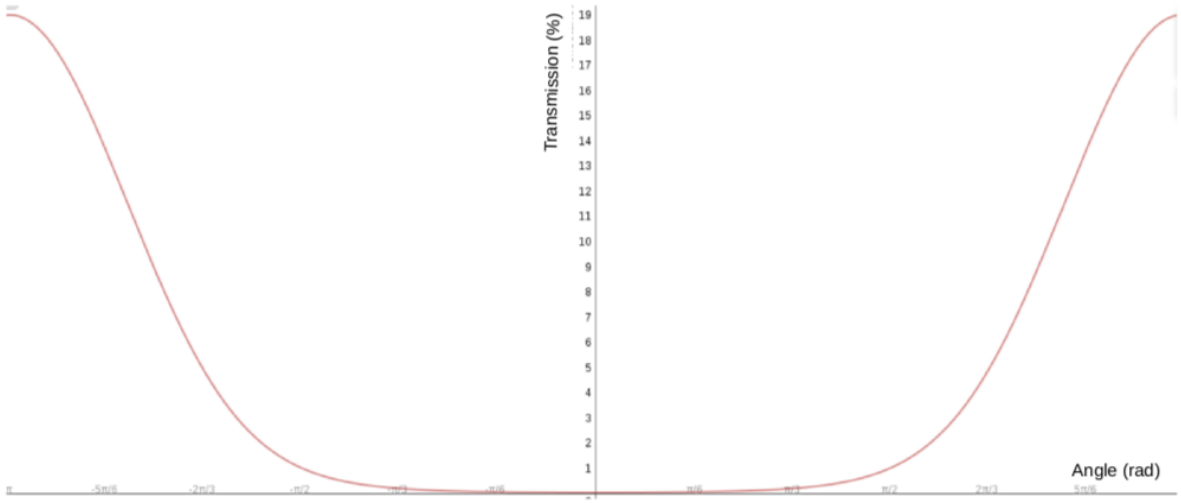

Figure 2.2 Simulation of Fresnel Reflection of TE Wave on SU-8

The Fresnel loss caused by the reflection of a wave by a material of higher refractive index increases exponentially with angle, as shown in Figure 2.2. So long as the angle is fairly shallow, the loss is relatively small, usually a fraction of a percent. If the difference in index of refraction is great enough, a large angle of incidence can reflect nearly all of the light.

In addition to unwanted reflection, light can miss the waveguide entirely. To estimate this loss, a number of equations must be considered. Lateral misalignment (if the profiles of the fibers and waveguide do not overlap):

$$\eta = \frac{2}{\pi}\left(cos^{-1}\frac{d}{2a} - \frac{d}{2a}\sqrt{1-\left(\frac{d}{2a}\right)^2}\right) \tag{2.28}$$

Angular misalignment (if the fiber and waveguide are not flush):

$$\eta = 1 - \frac{n_0 \theta}{\pi(NA)} \tag{2.29}$$

End separation (if the fiber and waveguide are not touching each other):

$$\eta = 1 - \frac{x(NA)}{4an_0} \tag{2.30}$$

Core mismatch (if the core diameter of the second fiber or waveguide is smaller than the first)

$$\eta = \frac{a_2}{a_1} \tag{2.31}$$

Numerical Aperture mismatch (if the second waveguide has a lower NA)

$$\eta = \frac{NA_2}{NA_1} \tag{2.32}$$

For all equations above, n_0 is the refractive index of the material between waveguides, a is the diameter of the fiber or waveguide, NA is the numerical aperture of the waveguide,

$$NA = \sqrt{n_{core}^2 - n_{clad}^2} \tag{2.33}$$

and x is the distance between waveguides along the propagating axis. It is important to note that

the core mismatch (2.29) and NA mismatch (2.30) are always zero if the receiving fiber is larger and has a higher NA, respectively [7]

2.3 Waveguide Propagation Losses

As one would expect, light may not propagate forever inside a waveguide. Some amount of loss is guaranteed just from traveling through a waveguide, regardless of how ideal it is. All forms of propagation loss fall into one of three categories: scattering, absorption, and radiation.

Scattering losses come in two forms: volume and surface. Volume scattering is almost impossible to predict theoretically, caused by small imperfections in the volume of the waveguide like bubbles, trapped solids, or unevenly cured polymer. This loss varies from sample to sample of a material, depending on the manufacturing conditions. Fortunately, this type of loss is typically very small relative to the other sources of loss. Because of this and the futility of describing it theoretically, this loss is often completely ignored.

Scattering loss may also result from surface scattering. Surface scattering is caused by rough waveguide surfaces. Scattering loss is usually the dominant propagation loss in dielectric materials like glass or polymers. Fortunately, it is also very easy to calculate. The loss from surface scattering depends on the number of times the wave contacts the surface

$$N = \frac{L}{2t_g cot\theta_m} \tag{2.34}$$

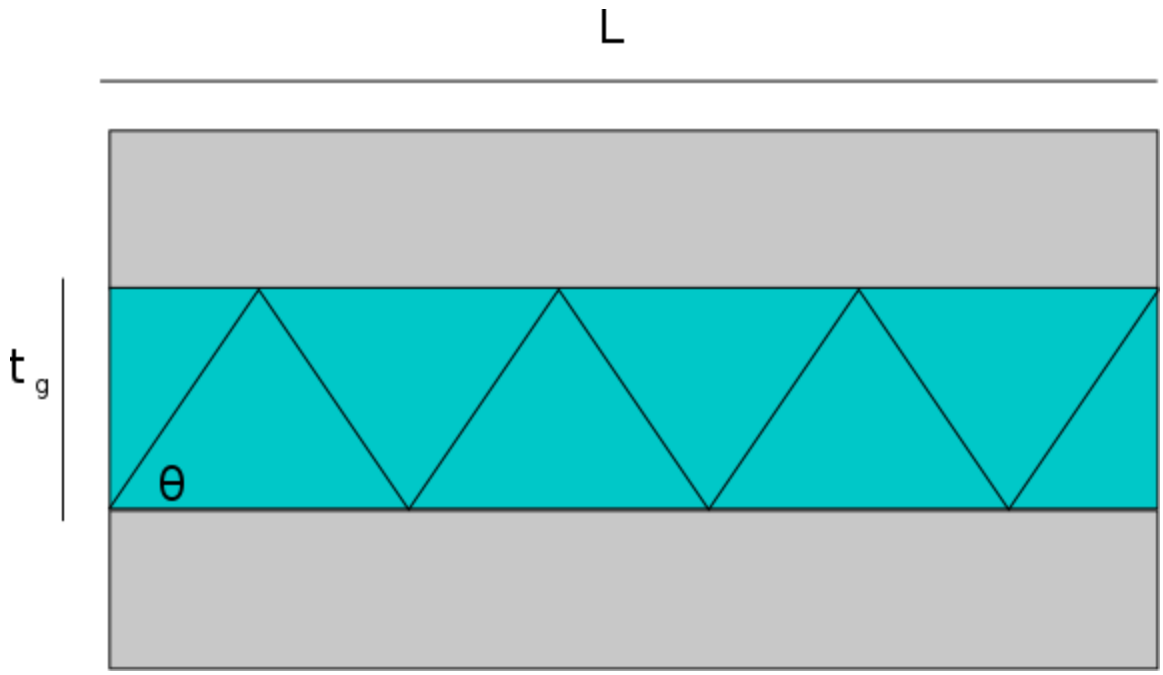

Figure 2.3 Geometrical Diagram of Surface Scattering Losses in a Waveguide

The scattering loss coefficient from surface scattering relates directly to the number of times the wave impacts the surface. This number of collisions is easily calculable from the geometry of the wave's propagation through the guide, as shown in Figure 2.3.

The surface scattering loss can then be calculated simply by the set of equations

$$\alpha_s = A^2 \left(\frac{1}{2}\frac{cos^3\theta_m}{sin\theta_m}\right)\left(\frac{1}{t_g+\frac{1}{\gamma_1}+\frac{1}{\gamma_2}}\right) \tag{2.35a}$$

where

$$\gamma_1 = \sqrt{\beta^2 - n_1^2 k^2} \tag{2.35b}$$

$$\gamma_3 = \sqrt{\beta^2 - n_3^2 k^2} \tag{2.35c}$$

$$A = \frac{4\pi}{\lambda}(\sigma_{12}^2 + \sigma_{23}^2)^{1/2} \tag{2.35d}$$

and $n_1 n_3$ are the refractive indexes of each side of the cladding (if different) and σ_{12} σ_{23} are the variances of the surface roughness between the waveguide and each cladding surface (if different).

Absorption loss comes from the waveguide material itself. Again, there are two distinct types of absorption loss. Inter-band absorption is simply a property of the material. As light strikes the material, some amount of it is absorbed in electron excitation events. Fortunately, this loss is easily avoided by simply choosing a waveguide material with loss inter-band absorption in the operating wavelength. Free-carrier absorption is a loss form almost unique to semiconductor waveguides. It represents the excitement of a free electron by incoming light. It is calculable by using the Fermi-Dirac distribution to estimate the number of electrons capable of absorbing the incident photon.

Radiation loss occurs as a result of light "seeping" from the waveguide. Under ordinary conditions, this loss is entirely negligible. However, if the waveguide is bent, this loss may become significant. When a wave turns inside a waveguide, the wavefront must be maintained. This means that the wavefront on the outside edge would have to travel faster than the wavefront on the inside edge, an obvious impossibility in a homogeneous waveguide. When the outside wavefront begins to lag, it can "fall of" the guided mode. This happens when the distance between mode segments exceeds the coherence length

$$Z_c = \frac{a^2}{2\lambda_1} \qquad (2.36)$$

where a is the width of the waveguide. It is possible to calculate the loss coefficient for a round bend from first principles, but it is more common to do so from empirical data by taking

$$\alpha_r = C_1 e^{-C_2 R} \tag{2.37}$$

where C_1 and C_2 are constants relating to the difference in propagation constants of the cladding and the core.

Radiation losses can also occur from other types of bending. Sharp angle bends like those found in star couplers and Mach-Zehnder interferometers also cause radiation loss. However, a theoretical estimation of this loss is exceptionally difficult. The best way to measure this loss is with experimentation. [8]

2.4 Dispersion in Guided Waves

Since modes propagate at different velocities, it is only natural that nearby modes separate as they travel through a waveguide. This relation is known as material dispersion and can be found by the dispersion relation

$$tan^2\left(\frac{d}{2}\sqrt{\frac{\omega^2}{c_1^2} - \beta^2} - m\frac{\pi}{2}\right) = \frac{\beta^2 - \omega^2/c_2^2}{\omega^2/c_1^2 - \beta^2} \tag{2.38}$$

where c_1 is the dispersion in the core and c_2 is the dispersion in the cladding. In practice, the material dispersion is condensed into a simpler relation

$$D_\lambda = \frac{-\lambda_0}{c_0}\frac{d^2 n}{d\lambda_0^2} \quad (2.39)$$

where c_0 is the speed of light in a vacuum. The dispersion coefficient D is reported in units of ps/km-nm. A smaller dispersion coefficient indicates a waveguide that may carry its signal for longer without degradation [7].

The shape of a waveguide may also provide another source of dispersion. Any bend in a waveguide necessarily causes dispersion as the leading edge of the wave travels faster than the trailing edge, as explained in Section 2.4. In general, the dispersion encountered by a wave undergoing a bend is

$$c_1 = R\frac{d\theta}{dt}[8] \quad (2.40)$$

Naturally, a hard-angle turn will possess a large time-derivative of the turning angle, leading to an enormous dispersion. This, in addition to the radiation loss caused by such turns, means that most curves are designed to be as gentle as possible.

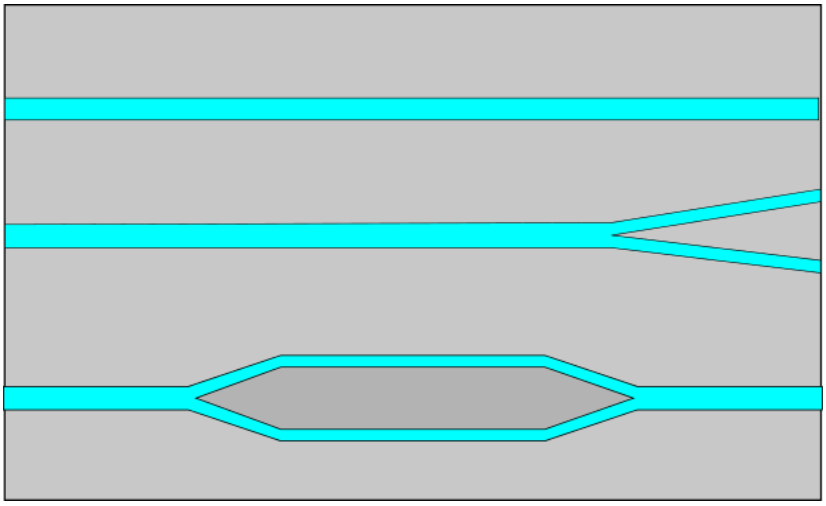

Figure 2.4 Various Waveguide Geometries

A straight waveguide (top), y-branch (middle), and Mach-Zehnder (bottom) are shown in exaggerated scale in Figure 2.4. Straight waveguides suffer only from material dispersion, while angled and bent waveguides are also subject to dispersion caused by the shape of the waveguide [8].

2.5 The Lorentz Model

The development of a theoretical framework for elecromagnetic waves in metals starts with an extremely simple mechanical model. In the Lorentz model, the motion of an electron is likened to that of a spring-mass system, with the electrostatic forces constraining the electron working much the same as the mechanical forces restraining the mass.

$$-q\tilde{E} = m\frac{\partial^2 \tilde{r}}{\partial t^2} + m\Gamma\frac{\partial \tilde{r}}{\partial t} + m\omega_0^2\tilde{r} \tag{2.41}$$

Here, as in the mechanical model, the second term represents a resist force (here, loss), and the

third term a restorative force. If the electric field oscillates harmonically with time (as is the case for light), the Fourier transform of this equation is more often used.

$$-q\bar{E} = -m\omega^2\bar{r}(\omega) - i\omega m\Gamma\bar{r}(\omega) + m\omega_0^2\bar{r}(\omega) \tag{2.42}$$

This is then solved for r, which then allows us to express the Lorentz form of the dipole moment.

$$\bar{r}(\omega) = \frac{-qE}{m(\omega_0^2 - \omega^2 - i\omega\Gamma)} \tag{2.43}$$

$$\bar{\mu}(\omega) = -q\bar{r}(\omega) = \frac{-q^2\bar{E}}{m(\omega_0^2 - \omega^2 - i\omega\Gamma)} \tag{2.44}$$

Since the polarization of a material is defined as the average dipole moment, this becomes

$$\bar{P}(\omega) = \frac{-Nq^2\bar{E}}{m(\omega_0^2 - \omega^2 - i\omega\Gamma)} \tag{2.45}$$

where N is the density of electrons.

Polarization can also be defined in terms of permittivity and electric field.

$$\bar{P} = \epsilon_0(\epsilon_r - 1)\bar{E} \tag{2.46}$$

In addition to making this substitution, it is common to collapse a term (2.44), giving

$$\epsilon_r = 1 + \frac{\omega_p^2}{\omega_0^2 - \omega^2 - i\omega\Gamma} \tag{2.47}$$

$$\omega_p^2 = \frac{Nq^2}{\epsilon_0 m} \tag{2.48}$$

This new term (2.42) is referred to as the plasma frequency of the material. This frequency is an inherent property of all materials and of particular importance to metals.

2.6 The Drude Model

While the Lorentz model reasonably depicts the oscillation of electrons in a material, further simplifications can be made when only metals are considered. Due to the high mobility of electrons within a metal, the restorative force and thus the resonant frequency can be ignored.

$$\epsilon_r = 1 - \frac{\omega_p^2}{\omega^2 + i\omega\Gamma} \tag{2.49}$$

This is referred to as the Drude equation and links permittivity and the frequency of incident radiation in a way that is easy to see and understand. The imaginary portion of the permittivity is directly proportional to the loss of the material and is commonly referred to as the extinction coefficient. It is easy to see that the closer the frequency comes to the plasma frequency of the metal, the lower the loss becomes. At frequencies above the plasma frequency, it becomes entirely transparent. More importantly, this means that the permittivity is negative so long as the frequency of the radiation is lower than the plasma frequency.

2.7 Surface Plasmon Resonance

When an electric field enters a metal, the free electrons move to a position of lower potential. This creates a charge imbalance in the metal, producing an electric field, which resists

the movement of electrons. As electrons continue to migrate, this electric field grows in strength until it cancels out the electric field that induced the shift. In this way, bulk metals almost instantly cancel out any electric fields inside their bodies.

What happens, though, if the metal is extremely thin and the electric field oscillates very quickly? The electrons can then move in time with the incident wave, mirroring its movement exactly as the wave travels over the surface. This process is known as surface plasmon resonance (SPR). By this mechanism, the oscillations in the metal and the elecromagnetic wave become inextricably linked, confining the optical wave to the surface of the metal. Waves so confined are referred to as surface plasmon polaritons (SPP).

This process does not happen every time light is incident on a metallic thin film. As with all coupling interactions, certain conditions must be met for the electromagnetic wave to be trapped as an SPP. As with more conventional waveguide coupling, the two waves may be compared by analyzing their wave vector. The wave vector of an SPP is described in terms of the original wave vector, the permittivity of the metal, and the permittivity of whatever dielectric it was traveling through.

$$\bar{k_p} = k_0 \sqrt{\frac{\epsilon_m \epsilon_d}{\epsilon_m + \epsilon_d}} \tag{2.50}$$

The permittivity of the metal is variable with respect to frequency, as predicted by the Drude model. Since the permittivity of the metal is negative, for the wave vector of the SPP to be real, the metal's permittivity must be greater (absolutely) than that of the dielectric. However,

as a result, the wave vector of the SPP is greater than that of the original wave. Since the momentum of a photon is directly proportional to the wave vector (related by the reduced Planck constant), this means that the momentum of the SPP is greater than that of the photon that produced it. It would appear at first that this increase in momentum would make coupling to an SPP completely impossible. There are, however, some circumstances under which this is possible.

The wave vector of the SPP and the incident wave above are only expressed in a single dimension, along the optic axis. As such, the momentum mismatch is not in the total momentum (which would be irreconcilable), but rather only the in-axis (z) momentum. By sacrificing momentum along one axis (x or y), it is possible to increase the on-axis momentum enough to meet the coupling conditions.

This can be achieved in a waveguide where an interstitial dielectric separates the waveguide from the metal. Waves that are totally internally reflected inside a dielectric are not truly totally reflected. Since continuity must be maintained at the boundary, a small amount of power must "seep" through in a tunneling process. This small portion of the wave will then propagate through the second dielectric, changing wave vector to have either a lower or higher momentum in the z axis. If this second dielectric possesses a lower refractive index, the momentum will increase, often enough to bridge the gap and couple into the metal layer [9].

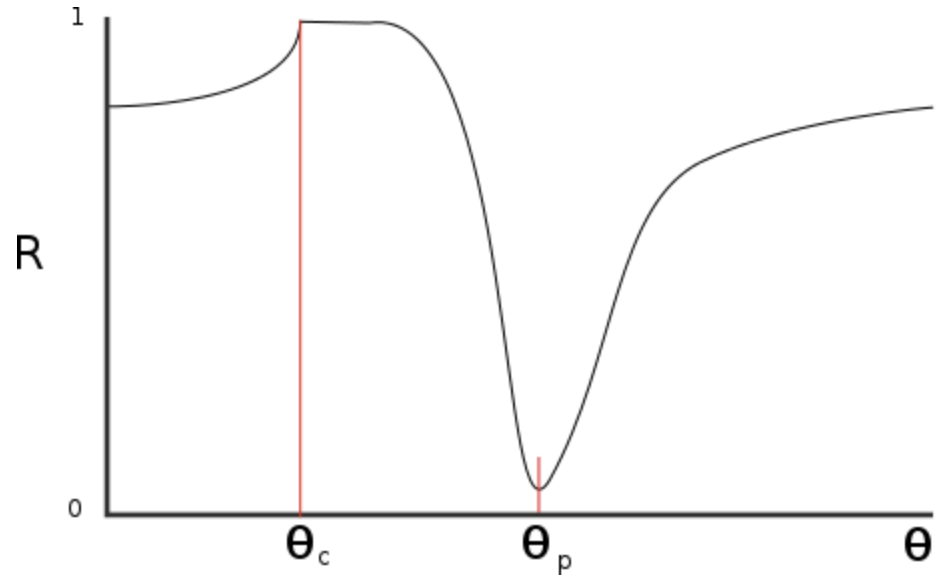

Figure 2.5 Form Sketch of Plasmonic Reflection With Respect to Angle of Incidence

Figure 2.5 shows reflection of an ideal plasmonic surface with respect to angle of incidence. The reflection increases up to the critical angle. Immediately past the critical angle, the reflectance stays near 1, as the classical model would predict (the wave is undergoing total internal reflection). As the angle increases, however, the momentum mismatch closes, allowing for the excitation of surface plasmons. This results in a steep drop of reflectivity until it reaches a minimum at the plasmon angle, at which point the surface is nearly totally transparent. As the angle increases thereafter, the coupling becomes less efficient, leading to an increased reflectivity as plasmons are no longer excited.

3. Fabrication of SU-8 Waveguides

Selection of the material used to form the waveguide was one of the most important considerations in the design of the test sample. Many polymers are available that provide favorable optical properties at 633 nm, so this was almost a non-issue. The greatest concern was selecting a polymer that would be easy to use, resistant to damage, and able to create crisp and clean waveguides.

The overwhelming favorite polymer waveguide in optics research is SU-8. It is reasonably transparent across a wide range of wavelengths, extending from infrared through the entire visible spectrum. It is a UV-curable negative photoresist, meaning that waveguides can be fabricated by a simple photolithography process. It is extremely durable, resistant to practically every chemical, and has good adhesion to glass and silicon. It is also capable of achieving vertical sidewalls with aspect ratios greater than 10:1 [10]. Moreover, its optical attenuation at 633nm has been studied extensively [11]. As such, it was a simple matter to select it as the material of choice for fabrication of the waveguides.

Table 3.1 Refractive Index of SU-8 [11, 12]

Wavelength	365nm	633nm	1550nm
Refractive Index	1.640	1.596	1.575

Table 3.2 Physical Properties of SU-8 [13]

Property	SU-8 3000
Softening Point, DMA (°C)	200
Thermal Stability in Nitrogen, Onset/5% Weight loss (°C)	277/357
Young's Modulus (GPa)	2.0
Coefficient of Thermal Expansion (ppm/°C)	52
Tensile Strength (MPa)	73
Elongation at Break (%)	4.8
Thermal Conductivity (W/mK)	0.2
Viscosity (cSt)	12000
Density (g/mL)	1.153

SU-8 is produced commercial by Microchem and available in a number of formulations with different solvents to fill various roles. The primary distinction between formulations is the viscosity of the mixture, which directly affects the maximum and minimum layer thickness. Initial fabrications were performed using SU-8 5, one of the thinnest available formulations. It was selected for its fast processing, a necessary consideration when simply learning the material's quirks and refining the fabrication process.

However, SU-8 5 is limited to a maximum single-layer thickness of about 30μm. A number of proof-of-concept tests were carried out with samples crafted from a pre-existing photomask in an attempt to determine the viability of the material. These early tests were unsuccessful. There were no difficulties with insertion, but the signal was completely destroyed before extraction by passive losses in the waveguide. In order to obtain a signal, more power needed to be delivered to the sample. This required using a thicker insertion fiber, which in turn necessitated a larger waveguide to match.

Due to the cost of SU-8 photoresists, it was determined that a single resist would need to be used for all further experimentation. In order to ensure that a waveguide of any size could be fabricated, SU-8 3050 was selected. With a thickness of 50μm to 100μm possible with a single coat, it provided the greatest range of manufacturing dimensions. All samples used and presented herein utilize SU-8 3050 for the fabrication of surface-mounted waveguides.

The resinous structure produced by the development of SU-8 is a Bisphenol A Novolac epoxy. It is from this polymer that the commercial formulation derives its name, a reference to the eight epoxide groups that partially comprise its structure. This polymer is closely related to a number of other resins used in more familiar commercial applications like pool balls, chemical-resistant countertops, and fiberglass. The SU-8 mixture also contains 10% Triarylsulfonium/hexafluoroantimonate by weight to produce photoacids [10], as well as a solvent unique to the formulation.

When SU-8 is exposed to ultraviolet light in the area of 365nm, the released photoacids spur the polymerization process, turning the viscous fluid into a solid polymer. As a negative photoresist, the areas exposed to ultraviolet light harden, while the areas not exposed can be removed by an appropriate developer. While a number of developers exist for SU-8, all samples were fabricated using Microchem's SU-8 developer. Additional baking after development can promote further cross-linking, producing a significantly harder if slightly less transparent polymer.

SU-8 is an incredibly durable polymer, with a tensile strength of 73MPa when hardened.

It also has good adherence to glass and fused quartz, with an adhesion sheer strength of 23MPa and 80MPa, respectively. This can be further boosted by adhesion promoters or primers, though these may interfere with the optical properties of the waveguide [11]. As such, none were used. Although no studies have been made to quantify its adhesion to nichrome, later research steps indicate that it is extremely poor.

Crucially, SU-8 is known for its outstanding chemical resistance. Once hardened, it can only be removed by pyrolysis, molten salt, Piranha etch (discussed later), and a proprietary remover produced by Microchem. As a result, the sample may be cleaned repeatedly between steps with no ill effects. It is also non-toxic and technically safe to eat, at least when cured.

The optical transparency of SU-8 has been studied extensively over the 300-800nm range, an area extending from near-UV to near-infrared. Its absorbance decreases exponentially over this range. The first ten optical modes have well-documented losses. While there is no accepted standard value for propagation loss in large multi-mode waveguides, a figure in the range of 1.1dB/cm is consistent with most published literature [11]. The refractive index of SU-8 varies between formulations and processing conditions. With a long curing time (as typical of SU-8 3050), its refractive index at 633nm converges towards 1.595.

3.1 Control Sample Fabrication

The substrate used was a simple {111} p-type 100mm wafer. The orientation and doping of the silicon do not meaningfully impact the optical qualities of the sample due to an overriding oxide layer. The wafer was cleaned by the standard RCA method, first in the metal ion

removing bath consisting of 1:1:6 hydrochloric acid to hydrogen peroxide to deionized water at 70 degrees Celsius for ten minutes. The wafer was rinsed and dried before being subjected to the organic wash consisting of 1:1:5 ammonium hydroxide to hydrogen peroxide to water, also at 70 degrees Celsius. The washing process is necessary to ensure that the wafer is devoid of unwanted contaminants, not only so that the following fabrication steps are not interrupted by impurities, but also so that the furnace is not contaminated by foreign matter that may boil off during oxidation. [14]

In order to ensure proper confinement of the guided wave, a layer of silicon dioxide was thermally grown. Since the exact thickness and consistency of the oxide layer is not of particular importance, wet oxidation was determined to be the method of choice, since a trade-off of quality in exchange for a markedly faster reaction was favorable under these circumstances. Oxidation took place in a 1000 degree quartz tube furnace. Prior to insertion of the wafers, the tube was evacuated with a flush of nitrogen gas. During oxidation, water vapor and oxygen were supplied into the tube. The pre-oxidation nitrogen wash, mid-oxidation oxygen supply, and post-oxidation nitrogen wash were all performed with a flow rate of approximately .566 l/min.

To calculate a theoretical value of the oxide layer thickness, we may use the Deal-Grove model,

$$X_0(t) = \frac{-A+\sqrt{A^2+4(B)(t+\tau)}}{2} \qquad (3.1)$$

and begin substituting the appropriate values. Taking constant terms from *Introductory MEMS:*

Fabrication and Applications Table 2.4, (111) silicon oxidation, we see that the coefficients for wet oxidation are A=.252μm and B=.316μm^2/hr. We then calculate τ using

$$\tau = \frac{X_0^2 + AX_0}{B} \qquad (3.2)$$

where X is the initial thickness of the oxide layer, here assumed to be 10nm and A and B being the same constants as above. Substituting and calculating, we see that Tau is .008291hr. Solving the Deal-Grove equation with these parameters gives a final thickness of the silicon dioxide layer of .452 microns. For a (111) wafer with 10nm of native oxide, we obtain a theoretical oxide thickness of 452nm.

To determine the empirical thickness of the oxide layer, a Filmetrics F20 thin film measurement system was used. On each of the wafers used to produce final samples, ten data samples were taken, five on the outer half of the wafer, and five within. The location of data points was roughly a pair of concentric, regular pentagons. The measured film thickness was an average of 320nm across all points on all samples, with a standard deviation under 5.0nm for data points on each wafer.

The precise thickness of the oxide layer is not of critical importance. A variation of 5nm across a 10cm surface is not disruptive to a waveguide over 100μm in height. Additionally, the penetration depth of the evanescent waves, generally taken to be a third of the wavelength of confined light, is not deep enough to reach the silicon underneath by a margin of 100nm.

Fabrication of waveguides from SU-8 takes place in several steps, outlined here and in Table 3.3, and explained in greater detail below. The steps, in order, are pre-bake, deposition and spinning, soft bake, exposure, post-exposure bake, development, and hard bake. This section details the process used to fabricate the control sample. An additional step is required for the plasmonic samples and is detailed later.

A wafer prepared and detailed as above was used in every fabrication process. Since many of the wafers were stored overnight after oxidation, another RCA clean as described above was performed on the wafers. Afterwards, the wafer was dried in a muffle furnace at 300 degrees for half an hour. After being allowed to cool to room temperature, the wafer was heated upon a hotplate to 95 degrees over the course of a minute. This process is known as the pre-bake. This ensures that the resist flows smoothly and evenly across the surface.

Approximately 6ml of SU-8 3050 was deposited by pouring onto the center of the wafer. This is in excess of Microchem's suggested 4ml quantity due to the extreme thickness of the waveguide. Initial attempts to use 4ml did not obtain even coverage of the desired height. The amount used is very approximate, as accurate volume measurements of SU-8 3050 are practically impossible. Its viscosity is slightly greater than that of peanut butter and it is extremely sticky. Volumes in excess of 1ml would adhere to the walls of a 10ml beaker. As such, the beakers were simply filled and an amount dispensed to empty more than half of the container. An attempt was made to apply the resist by syringe for greater consistency, though each sample prepared this way suffered from an abundance of air bubbles, ruining the sample.

The spin cycle of the wafer needed to be modified to account for the fluctuating amount of resist. Following the Microchem data sheet with slight modifications, the following program was devised: accelerate to 500 rpm over 5 seconds, spin for 10 seconds; accelerate to 1000 rpm over 3 seconds, spin for 30 seconds; slow to 100 rpm over 3 seconds, spin for 5 seconds; slow to stop. This process created a smooth and mostly bubble-free coating of approximately 100μm for 4/5 attempts. Occasional errors occurred during this step. Any wafer deemed defective was washed with developer and thoroughly cleaned before being recycled to the beginning of this step.

It is also notable that an edge bead (thicker layer of resist around the edge) formed in every sample. This generally disappeared over the next several steps, the polymer flowing to seek its own level. Thin tendrils of SU-8 often formed around the perimeter of the wafer, flowing off and hanging midair. This was a result of the uncertain quantity of resist spun over the wafer. These aberrations were trimmed before the next step and had no bearing on further processing.

A soft bake is typically the longest step of any photolithography and mostly serves to drive off any dissolved gasses and evaporate the solvent. In this case, the soft bake also provided enough time for the spun resist to relax and settle evenly across the surface of the wafer, evening out the edge bead. The soft bake was performed in a muffle furnace at 95 degrees for one hour. Temperature control of muffle furnaces is not exactly precise, so each sample was baked with a ±2 degree tolerance. Since all soft bake times and temperatures are approximate for very thick SU-8 layers, it is not expected that this variance has any significant effect on the sample.

Exposure of the wafer was performed on a SUSS MJB4 aligner operating in soft contact mode. In soft contact mode, the wafer is pressed mechanically against the mask until contact is made. The piston then continues to press the wafer up until a certain force is applied. This quantity is called the wedge error compensation (WEC) pressure. It is intended to ensure that the wafer is pressed flat against the mask. Unfortunately, due to the stickiness of SU-8, this often caused the resist to stick to the photomask, ruining the sample and marring the surface of the mask. As a result, the WEC pressure was set to the device minimum. Even after this adjustment, more than half of all samples were irreparably damaged by this process and had to be cleaned and recycled. This likely caused slight discrepancies in the width of waveguides across their length, though the greatest measured difference was under 100nm (measured by SEM), a small aberration to such a large waveguide and well within the manufacturing constraints.

Wafers and masks marred by hard contact were cleaned by Piranha etch, an extremely aggressive wet chemical etch using concentrated sulfuric acid and hydrogen peroxide at 95 degrees. The solution does not harm glass or chrome (the material from which the photomask was made) but would readily dissolve even fully cured SU-8.

The exposure time used in each case was 30s, corresponding to an irradiation of 300mJ per square centimeter. This high exposure energy is to ensure that the SU-8 is exposed all the way through to the substrate.

Figure 3.1 SUSS MJB4 Mask Aligner With Partially Loaded Wafer

Figure 3.1 shows the wafer loaded into the mask aligner. After loading, the wafer and tray slide into the body of the aligner. The device automatically brings the wafer into contact with the mask, as prescribed by the WEC and exposure settings. Here, a soft contact with minimum WEC pressure was used. Once the desired pressure is reached, the wafer can be exposed.

A post-exposure bake is performed in order to stop the polymerization that begins during exposure and to prepare the resin for development. This bake was performed on a hot plate set to 95 degrees and lasting for five minutes, as prescribed by Microchem's data sheet. During this time, the outlines of the waveguides became visible. If this was not the case, the wafer was stripped and recycled to the beginning of the process.

An additional stress reduction bake was performed at 65 degrees for one minute after the post-exposure bake. This serves a dual purpose of reducing the brittleness of the waveguides and also ensuring a more even cross-linking of the SU-8 molecules, resulting in more consistent optical properties. The wafer was allowed to cool to room temperature before and after this process.

The samples were developed in Microchem's SU-8 developer. A high-walled dish was filled with 25mL of developer and swirled gently for no less than fifteen minutes, until the features were clearly visible and no patches of unexposed SU-8 were visible on the surface and all the waveguide edges were crisp and clear. The large quantity of developer and comparatively long development time result naturally from the thickness of the SU-8 film.

After the first stage of development, the wafer was removed from the dish and immediately sprayed with isopropyl alcohol. This process dissolves the products of SU-8 development that would normally adhere to the surface. These reaction products are clearly visible in the rinsing step as cloudy white streaks that form wherever the alcohol travels. The wafer was then spun at high speed for twenty seconds to remove the dissolved contaminant. A water flush and another spin was then performed.

Following the alcohol rinse, the wafer was transferred to a petri dish with a small quantity of fresh developer and agitated gently for a minute. This step develops and removes any small amount of unexposed SU-8 that may have been protected by the reaction byproducts cleared in the previous step. This was immediately followed by another alcohol rinse, repeated until no

cloudy streaks are visible in the applied alcohol. When this was complete, the wafer was rinsed in water and spun to dry as above.

Typically, SU-8 is baked for an extended period to further cross-link the polymer and strengthen it. Unfortunately, it was discovered that this process decreases the transparency of the waveguides considerably and was neglected for all samples used for experimentation. Laboratory conditions are rarely strenuous enough to damage the waveguides.

Table 3.3: Process summary

Section	Step	Process	Effect
3.6.1	Pre-bake	300 degree 30 min oven bake, 95 degree 5 min hotplate bake	Dry and prepare substrate for spinning
3.6.2	Deposition and Spinning	6mL pour of SU-8 3050, 1000 rpm primary spin for 30 seconds	Coat the wafer with waveguide material
3.6.3	Soft Bake	95 degree one hour oven bake	Boil out gasses and liquid solvent
3.6.4	Exposure	30 seconds, 300mJ/cm, extremely low WEC	Solidify waveguides and protect from developer
3.6.5	Post-Exposure Bake	95 degree 5 min hotplate bake, 65 degree 1 min hotplate bake	Stop reaction, prepare for development
3.6.6	Development	15 minute soak, repeated isopropyl alcohol washes	Remove undeveloped SU-8, form waveguides
3.6.7	Hard Bake	None	Harden polymer; skipped due to deleterious optical effects

3.2 Fabrication of Nichrome Field

The experimental design required a layer of nichrome to cover the entire surface of the wafer, except directly underneath the waveguides. To achieve this, the nichrome was applied to the surface and then patterned in the process described below.

Nichrome was deposited via sputtering. A freshly cleaned and oxidized wafer was dried in a muffle furnace for half an hour before being placed into the sputterer. Sputtering was performed at a pressure of $9.1 \cdot 10^{-8}$ Torr (measured by integrated ion gauge) and a rate of 2.2 kÅ/s. The final thickness of the nichrome film was 20.0nm ±0.1nm, as measured by atomic force microscopy (AFM).

Figure 3.2 Full Sputtering System and Detail View of Loading Dock With Wafer

Figure 3.2 shows the sputterer (left) and the blank wafer locked into the loading chamber (right). After loading, the chamber is sealed and pumped down to hard vacuum. The sample is then inserted into the main chamber prior to sputtering. Figure 3.3 shows sputtering in progress. In the sputtering process, an inert gas (typically argon) is injected into the chamber and ionized. Positively charged ions are drawn toward the target (left) at high speeds. These collisions with the target knock atoms off its surface, launching them toward the substrate (right). When these free atoms strike the substrate, they adhere immediately, coating the surface in an extremely thin layer. Here, the target is a nichrome alloy.

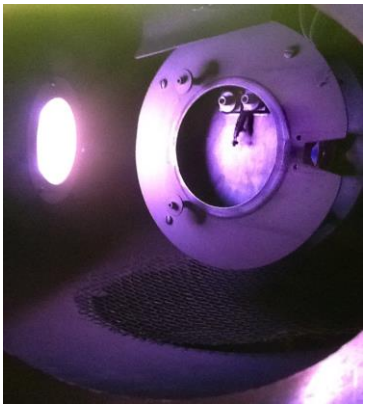

Figure 3.3 Nichrome Sputtering on Silicon Wafer

After coating the wafer with nichrome, the wafer underwent another lithography process, this time using an AZ-type positive photoresist. While a negative photoresist would leave material where the UV struck it, forming the waveguides, a positive photoresist would be eradicated where exposed, forming a cutout in the nichrome in the shape of the waveguides. This forms what is known as a field mask, a sacrificial layer meant to protect what is underneath. The process used for this lithography is very similar to the one described previously, except where noted below in Table 3.4.

With a field mask now protecting the nichrome important to the experiment, the remaining nichrome can be removed by wet chemical etching. Ceric ammonium chloride, nitric acid, and water were mixed to a ratio of 2:1:17 by mass. This is a particularly dilute mixture, so chosen to etch slowly. The wafer was immersed into a dish containing just enough etchant to cover the wafer and agitated at room temperature until the nichrome was visibly eradicated. Etching times varied but were consistently between 30s and one minute. After etching, the wafer was rinsed with water and spun dry. The field mask was then stripped by consecutive washes

with acetone, isopropyl alcohol, and water. The wafer was then cleaned by the RCA cleaning method described earlier.

Table 3.4: Photoresist Field Mask for Nichrome Patterning

Step	Process
Pre-Bake Deposition and Spinning Soft Bake	95 degree hotplate bake for 1min 4mL deposited, spun at 6500 RPM for 1min 95 degree hotplate bake for 5min
Exposure	4 second exposure
Post-Exposure Bake Development	95 degree hotplate bake for 1min Swirled in diluted AZ developer until pattern was clear, under a minute

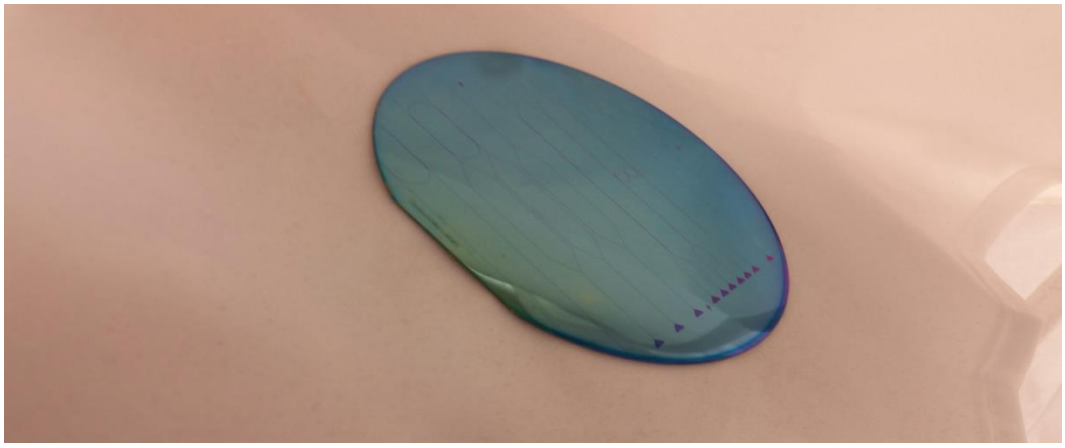

Figure 3.4 Sample Wafer after Patterned Nichrome Etch

The nichrome has been etched and the photoresist removed, as shown in Figure 3.6. The majority of the wafer is still covered in nichrome, giving it a gray tint. The waveguides are visible as dark, slightly purple lines. The color is due to the exposed oxide underneath the nichrome.

3.3 Fabrication of the Experimental Sample

Thicknesses achieved due to spin coating vary greatly with the adhesion between the surface and resist. When the nichrome field was added beneath the waveguide layer, the resultant thickness of the spun-on layer was significantly thinner than previous samples. As such, some modifications needed to be made in order to produce acceptable waveguides.

While SU-8 3050 is believed to be capable of spinning single-coat layers well in excess of 100μm, no data is available to predict the required spin cycle. As such, thicker coatings require multiple layers. There is virtually no published data to predict the thickness of multiple spun SU-8 3050 layers. The technique is, however, in use with other resists and known to be effective. As such, the deposition and spinning regime was kept simple. The first layer would be spun as above. The second layer would be poured directly atop the first and spun following the exact same procedure as above. In effect, the process described in 3.6.2 was simply performed twice, once on top of the other.

This method resulted in consistent waveguides with thicknesses approaching 300μm. Since the second layer of SU-8 is spinning atop an already deposited layer of SU-8, the thickness of the polymer layer did not vary significantly between those spun over nichrome and those spun

over bare silicon dioxide. The measured thicknesses for the samples used were 233.3μm and 232.8μm±0.1μm. These measurements were taken via surface profilometer.

The exposure time was also increased to one minute at the same intensity as before. Also, because the waveguides needed to go precisely over the tracks cut into the nichrome, the second lithography would need to be performed with an alignment. Precise controls built into the MJB4 allow the wafer to be positioned exactly in line with the mask. Alignment marks were built into the mask to make this process easier.

3.4 Summary

The overall process to create the sample is summarized in figure 3.5, split into six stages. In stage 1, the silicon dioxide layer is grown and the nichrome is sputtered over the entire substrate. This step can be seen in Figure 3.1. In stage 2, the AZ-type photoresist is spun over the nichrome. The resist is then patterned and etched in stage 3, leaving the wafer bare where the waveguides will be. The nichrome is then etched away in stage 4, using the remaining resist as a field mask to protect it from the etchant, as seen in Figure 3.3. In stage 5, the resist is removed, the surface cleaned, and the SU-8 spun to a thickness of 300 microns over the wafer. In stage 6, the SU-8 is exposed and developed, forming the completed waveguide. This can be seen in Figure 3.5. After this, the edges of the wafer were trimmed to fit the waveguides with an automatic wafer saw to leave a 10um gap between waveguide and edge. This is portrayed in Figure 3.6.

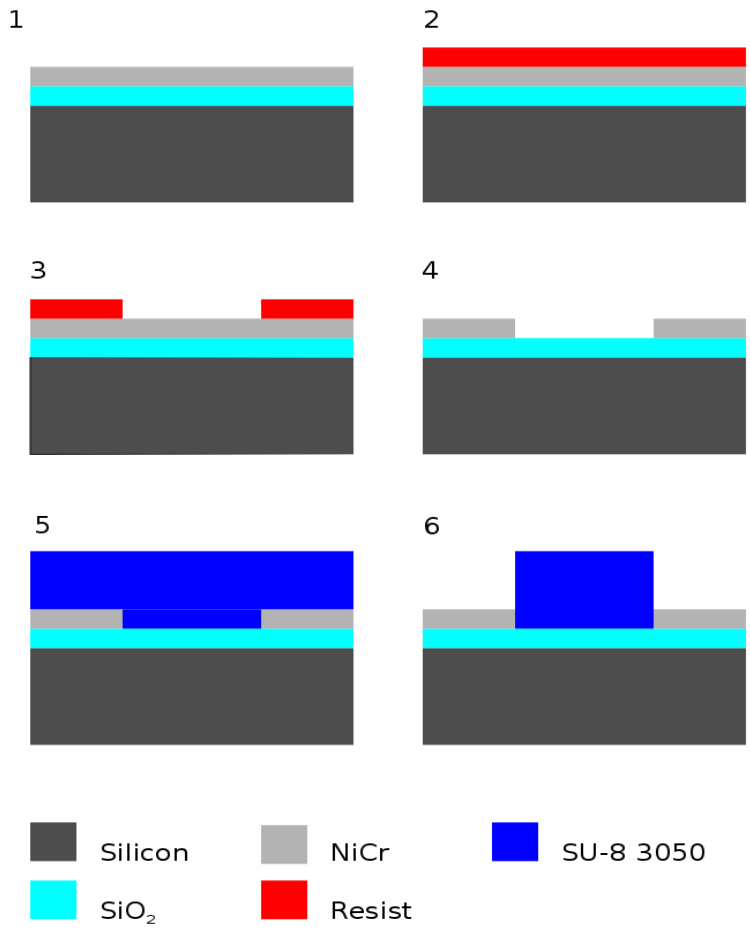

Figure 3.5 Experimental Sample Fabrication Process Flow

Figure 3.5 shows block diagram of the process flow that breaks the fabrication into significant steps. In step (1), the oxide is grown and the nichrome deposited. In (2), the field mask is applied. At stage (3), the field mask is developed, exposing the nichrome underneath. During stage (4), the remaining field mask is removed. In stage (5), the SU-8 3050 is spun on and prepared for development. Finally, the SU-8 is developed in step (6), completing the fabrication.

Figure 3.6 Automated Wafer Saw

Figure 3.6 shows the saw used to cut down the ends of the wafer. The wafer is locked onto the vacuum chuck in the center of the cutting platform and aligned with the cutting axis with aid from the emplaced microscope. Once the alignment has been made and the desired cutting program entered, a diamond blade slices the wafer to the desired depth, lubricated by a water spray. The wafer may then be broken along its perforation by a steady hand. This process was done on each side of the wafer.

The edges have been sawed off in Figure 3.7, leaving a scant 10um of wafer between the edge and the insertion wedge. The faint lines visible on the inside of the Mach-Zehnder are shadows cast by the waveguide.

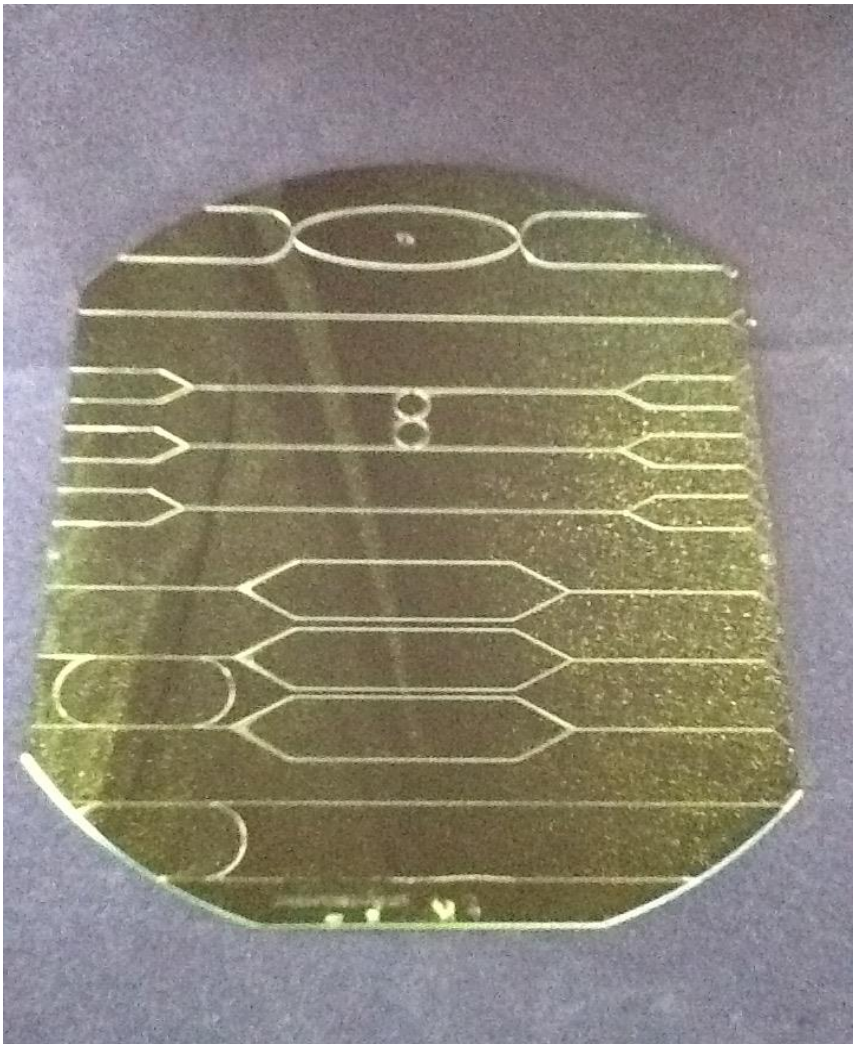

Figure 3.7 The Finished Experimental Sample

3.5 Mask Design

In order to perform photolithography, a mask must be designed and created to produce the required sample. The mask was designed in AutoCAD 2014 and produced by Photo Sciences Incorporated. The mask was produced with a tolerance of 0.5μm and a critical dimension (smallest possible linewidth) of 3.0μm. The material is chrome on soda lime glass. The mask is designed to work on standard 4" aligners.

Figures 3.8 through 3.11 depict the whole or portions of the mask. All dimensions are given in millimeters. The waveguides are uniformly 100μm wide. Figure 3.8 depicts the full mask. The devices, from top to bottom, are the U-bend, straight line, paired 2x2 star couplers, 2x2 star coupler, Mach-Zehnder, coupled Mach-Zehnders, coupled straight lines. Only the straight line and Mach-Zehnder are actually used. The wide triangles on the left of each waveguide are the insertion wedges, shown in detail below. There are also seven alignment marks visible on the mask.

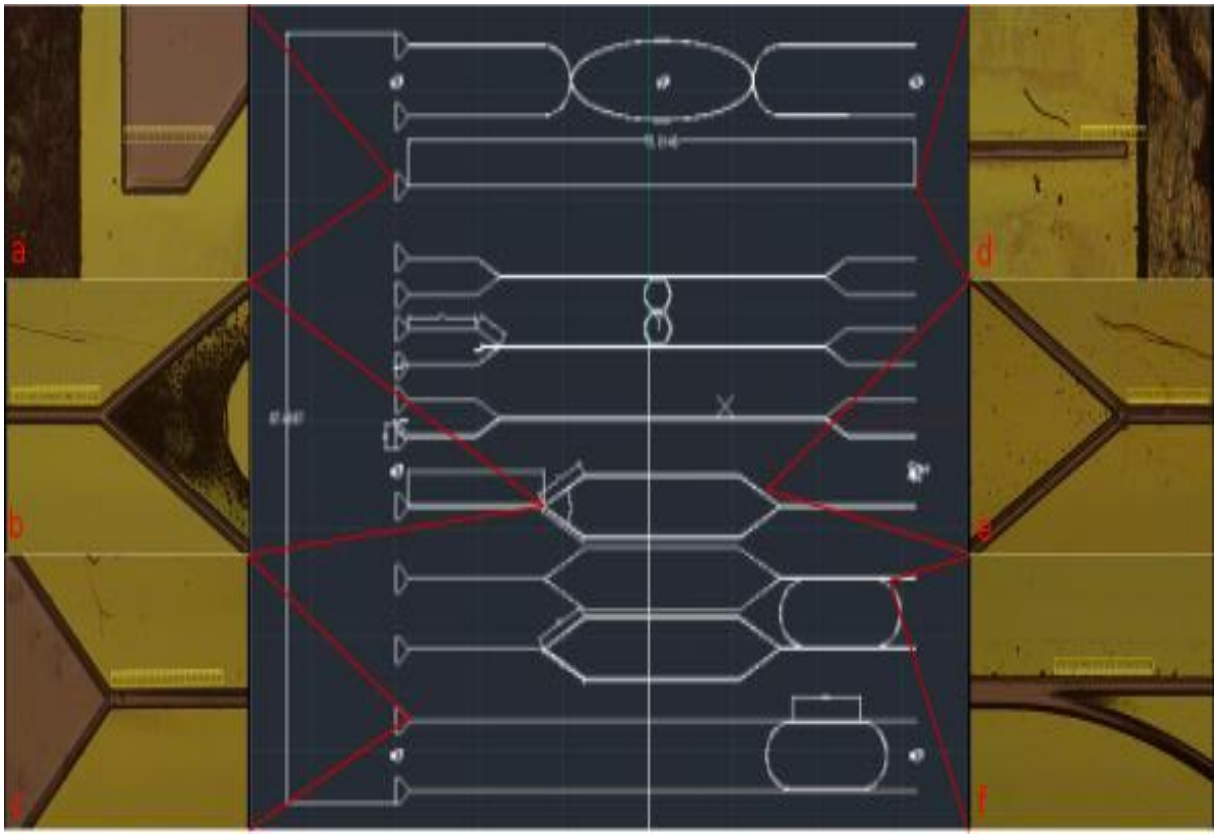

Figure 3.8 CAD Diagram of Photomask with Optical Microscopy Detail Images of Key Points

Figure 3.8 shows the final design sent for fabrication. All units are in millimeters. Alignment marks can be found around the U-bends, underneath the lone star coupler, and between the arms of the coupled lines. Annotations are visible, showing the dimensions of the components. The U-bend consists of two waveguides joined by an ellipse. The straight waveguide is a single, uninterrupted waveguide. The 2x2 couplers consist of two outwards-facing y-bends meeting at a 60° full angle. Two sets of 2x2 couplers are joined by a pair of circulating rings. The Mach-Zehnders consist of two inwards-facing y-bends, meeting at a 60° full angle. Two Mach-Zenders are joined by an extended circulating ring. Figures 3.10a-3.10f show microscopic images of key points on the fabricated wafer. The great deal of black residue on 3.10b is simply debris collected inside the bend, as this spot is difficult to clean.

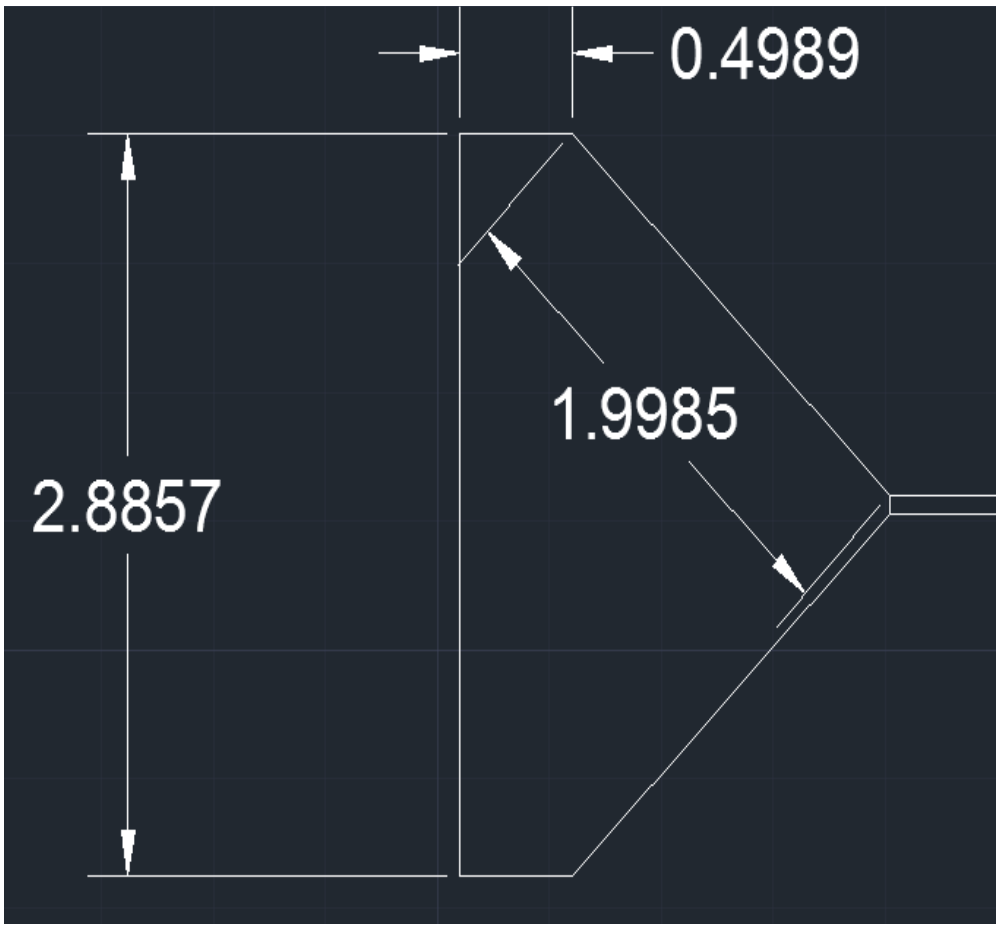

Figure 3.9 CAD Diagram of Waveguide Insertion Wedge

Figure 3.9 shows a detail view of the insertion wedge with annotations in millimeters. The insertion wedge facilitates coupling by making serious misalignment virtually impossible.

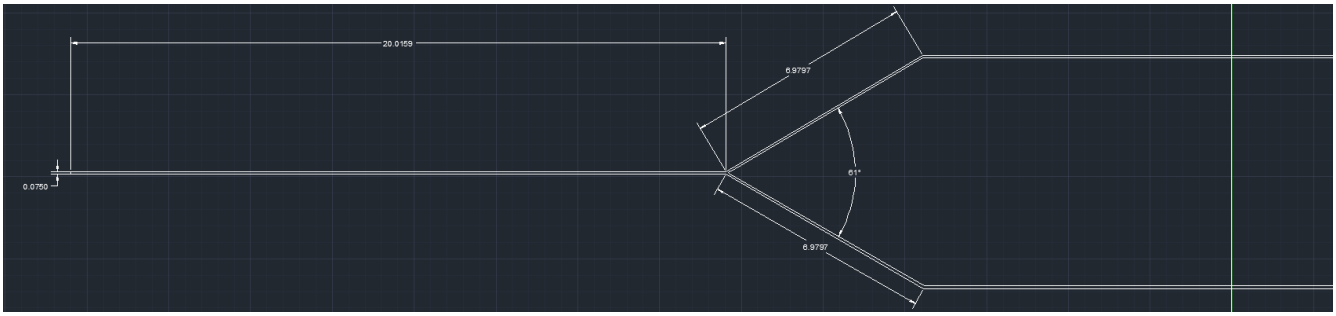

Figure 3.10 CAD Diagram of the Extraction Side of a Mach-Zehnder

The Mach-Zehnder is shown in detail in Figure 3.10 with annotations in millimeters. The split in the Mach-Zehnder is extremely sharp, a hard 60 degree full-angle bend. This component is reflexively symmetric about its center, disregarding the insertion wedge.

The alignment mark is illustrated in Figure 3.11 with annotations in millimeters and pictured below, viewed at 2.5x magnification through a micromanipulator. The alignment mark is intentionally asymmetrical about any axis. The arms of the crosses are also of different width and height. This was done to provide the most reference points possible. Aligning a mask can be difficult and the process is significantly easier if aided by an asymmetrical alignment mark.

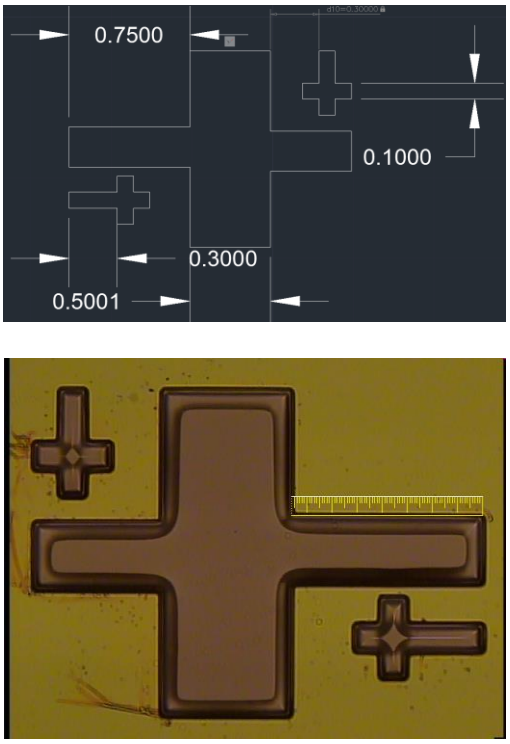

Figure 3.11 CAD Diagram and Optical Microscopy Image of Alignment Mark

4. Experimental Characterization

4.1 Overview

The first requirement was that the experimental apparatus be user-friendly. The ability to determine whether or not it was working properly at a glance was considered paramount. Using a light source visible to the human eye would make it easier to ensure that the light was being inserted and extracted as expected. As a result, the operating wavelength was restricted to 632.8nm. This wavelength alone satisfied the wavelength requirement for inducing SPR in nichrome, is visible to the human eye, and was readily available due to the ubiquity of moderate-power helium-neon lasers.

Light then needed to be inserted into the waveguide. Prism and grating coupling was considered but ultimately rejected due to lack of availability of appropriate resources. This necessarily restricted the method of insertion to either fiber butt-coupling or direct insertion from a free-space laser. Due to the relative ease of free-space-to-fiber coupling, it was determined that butt coupling would be ideal.

Extraction of signal was to be achieved by free-space coupling to the detector. In other words, extraction is performed by simply allowing the light to come out of the waveguide. The wafer was also cleaved nearly flush to the trailing edge of the sample to ensure that the detector could be placed as close as possible.

4.2 Description of Data

Data was taken in the form of optical power measurements provided by a photodetector (detailed below). All measurements were on the order of micro watt. Measurements were taken on both the control sample and the experimental sample for both straight line waveguides and Mach-Zehnder waveguides.

4.3 Using the Model

Since the intention of this experiment is to generate excessive loss, it is important to first estimate the inherent loss of the system. Losses caused by sharp angle bends are extremely hard to predict theoretically, but the other losses can be accounted for easily. See Chapter 2 for a theoretical description of coupling losses.

Fresnel reflection provides a small amount of loss based on the refractive index of the materials and the angle of incidence. For unpolarized light (used in this experiment), the average of the TE and TM reflection is taken. As is immediately obvious, for very small angles, this reflected power goes to zero. With a very liberal estimate of a five degree offset, the reflections upon insertion are 5.308% and 9.590% for s and p polarization, respectively. This gives an unpolarized reflectance of 7.449%, or -0.336dB, which will be more convenient later on. The reflection at extraction is practically nonexistent, less than a thousandth of a percent. In addition to unwanted reflection, light can miss the waveguide entirely. To estimate this loss, a number of equations must be considered, presented in Chapter 2.

At first, geometric coupling losses may appear to be a source of considerable loss, considering the number of mechanisms. However, it is often possible to eliminate many or all sources of coupling error by choosing the correct fiber and waveguide.

By design, the sample waveguide is dramatically larger than the insertion fiber, twice as large in its smallest dimension and six times as large in its largest. This provides an enormous advantage in eliminating coupling losses. The core mismatch (5.6) can be eliminated completely, as there is no loss if the receiving waveguide is larger than the transmitting one. Lateral misalignment can also be ignored, as it would require the fiber to be misaligned by a distance greater than its own diameter for it to incur loss.

Similarly, the numerical aperture mismatch can be ignored so long as the waveguide's NA is greater than that of the fiber. The NA of the waveguide is easily calculated.

$$NA = \sqrt{n_{core}^2 - n_{clad}^2} \tag{4.1}$$

The refractive index of the core is that of the SU-8, 1.595 at 633nm. The refractive index of the cladding is slightly more complicated, as both glass and air surround the waveguide. Assuming the worst, the refractive index of glass is used. This gives a numerical aperture of 0.88. The numerical aperture of the fiber, as listed by the manufacturer, is 0.19. As such, any loss from NA mismatch can be ignored.

This leaves only angular misalignment and end separation. Assuming again that the angular mismatch is around five degrees and using the NA of the waveguide calculated above, the loss from this misalignment must be less than 3.2%, or -0.141dB.

Ideally, the distance between the fiber and waveguide should be zero. During experimentation, the fiber was pushed into physical contact with the waveguide, so it is very likely that this loss is also zero. It is, however, possible that some distance did separate the two, possibly due to the above angular misalignment. Assuming that this is the case and any distance between the two is caused by a wedge alignment, the distance from core to core is approximately 5.5 μm, based on a cladding diameter of the fiber of 125μm. Using this figure, a loss of 0.261%, or -0.013dB is obtained.

Adding all of the above losses together, a sum of -0.490dB is obtained. This number represents a high water mark of loss, calculated using the worst-case reasonable scenarios. In all likelihood, the loss is considerably lower than this due to the methodology used to align the fiber and waveguide.

It is worth noting that it is assumed that there is no loss at extraction from the waveguide. The aperture through which light passes to hit the detector is so much larger than the waveguide that it would require an error of millimeters in order for loss to be observed. The great deal of care taken in collecting data obviates any chance of this being possible.

As mentioned previously, the multi-mode loss figure used in all calculations in this

research is 1.1 dB/cm. Conflicting literature indicates that the uncertainty is around 0.1 dB/cm (6). With a total length of 77.0 cm for the straight line, this gives a propagation loss of -8.5 dB, though it may be as high as -9.24 dB or as low as -7.7 dB. This error bracket is actually larger than the sum total of coupling losses, indicating that their contribution is indistinguishable from the natural losses incurred by transmitting light through SU-8. Even still, for the purposes of further calculations, a sum of -9.0dB will be used.

4.4 Optimizing Method

Due to the very uncertain nature of loss estimation for this system, it is of critical importance that solid experimental methodology be developed in order to ensure precise and accurate measurements. The system developed uses iterative adjustments to find the most accurate reading possible. This method was established after making a few basic assumptions about the data to be collected.

The first assumption is that all power measured comes directly from the waveguide. In order to ensure that this is the case, several steps were taken. First, as mentioned previously, a pinhole aperture was placed over the detector to remove the interference of other sources of light. Each measurement was taken with the lights off. No computer screens or “running lights” were left within the room and foam was placed under the door to block light from the hallway. The only light source in the room was the laser. This was confirmed by a null reading on the photodetector as long as it was not pointed towards the laser. Just in case, a solid barrier was placed between the laser and the detector to block any scattered light.

The second assumption is that any signal detected must have been transmitted through the waveguide. Therefore, all recorded measurements represent the power being coupled out of the waveguide at the current coupling conditions. As a result, in order to ensure the lowest coupling loss possible, only the highest recorded powers were saved and considered to be valid results. Any lower powers must be the result of higher-loss coupling conditions.

Since only the highest measurements taken actually count, a process was developed to obtain the highest possible power readings. Since so many degrees of freedom were available, in order to reach the true maximum power, adjustments must be made iteratively. This process is described in detail below and summarized in flowchart form in Figure 4.1.

After the sample was mounted and lifted to an appropriate height by the emplaced scissor jack, the photodetector was moved into position. It was placed nearly abutting the wafer, yet with enough space for some maneuverability. The photodetector was then raised or lowered until the pinhole crested the waveguide, ensuring that no light from the wafer was blocked, yet no extraneous light was allowed in. This process was done in a fully lit lab and not repeated until the sample was changed. A vacuum pump held the sample firmly in place once this process was completed and was not released until after all measurements were taken.

At this point, the insertion fiber was moved into position. Still in a well-lit room, the fiber was positioned as accurately as possible, utilizing a digital camera mounted above the apparatus (not visible in pictures) and a scope lined up to view from the side. These views together allowed for a precise three-dimensional alignment to be made, with the scope assisting

in vertical alignment and the camera providing a view from which the horizontal alignments could be made. The fiber was positioned just out-of-contact with the waveguide but aligned co-axially.

From this point forward, all other light sources were extinguished. The insertion fiber was moved along one axis at the slowest rate of speed possible while watching the readout provide by the photodetector. A full sweep of the waveguide was made from end-to-end, drawing the fiber across its width or height and observing the highest value spotted. Once the entire fiber was traversed, the fiber was returned to this local maximum. Once this was complete, the other available axis was treated the same way, sweeping across the full width or height of the waveguide before returning to the local maximum. At no point was the fiber in contact with the waveguide.

Once two axes were fixed to their local maxima, the fiber was slowly brought into contact with the waveguide. Contact was determined in several ways. Firstly, the stress from contact minutely deformed the tip of the fiber, causing a noticeable increase of scattering from the tip. Once this occurred, the fiber dial was reversed at the slowest possible speed until this effect disappeared. At this point, the lights were switched back on and another look was taken through the scope and the camera. This way, it could be confirmed that the fiber was indeed in contact, to the limit of the resolution of the devices.

The light was then extinguished and a preliminary reading was taken and written down (still in the dark). Next, one of the two non-propagation axes were adjusted at a slow speed,

making note of trends in measured power. When a local maximum was again encounter, this number was recorded and the other axis manipulated until a maximum value was obtained. At this position, the fiber was slowly pushed closer to the waveguide and then back, writing down the highest value achieved. This value was considered a potential data point. The fiber was then returned to soft contact and this step was repeated several times. This step generally took about an hour to produce a single data point, the highest value of the potential data points.

At this point, the fiber was backed off completely and the position scrambled in order to ensure that the process was performed properly, from the beginning, each and every time. With the lights on once again, all potential data points were transcribed to another piece of paper and recorded permanently. It was discovered early in the experimental process that one with exceedingly poor handwriting should not attempt to scribe data in the dark. Once this was complete, the process was repeated from the first stage of aligning the fiber by eye.

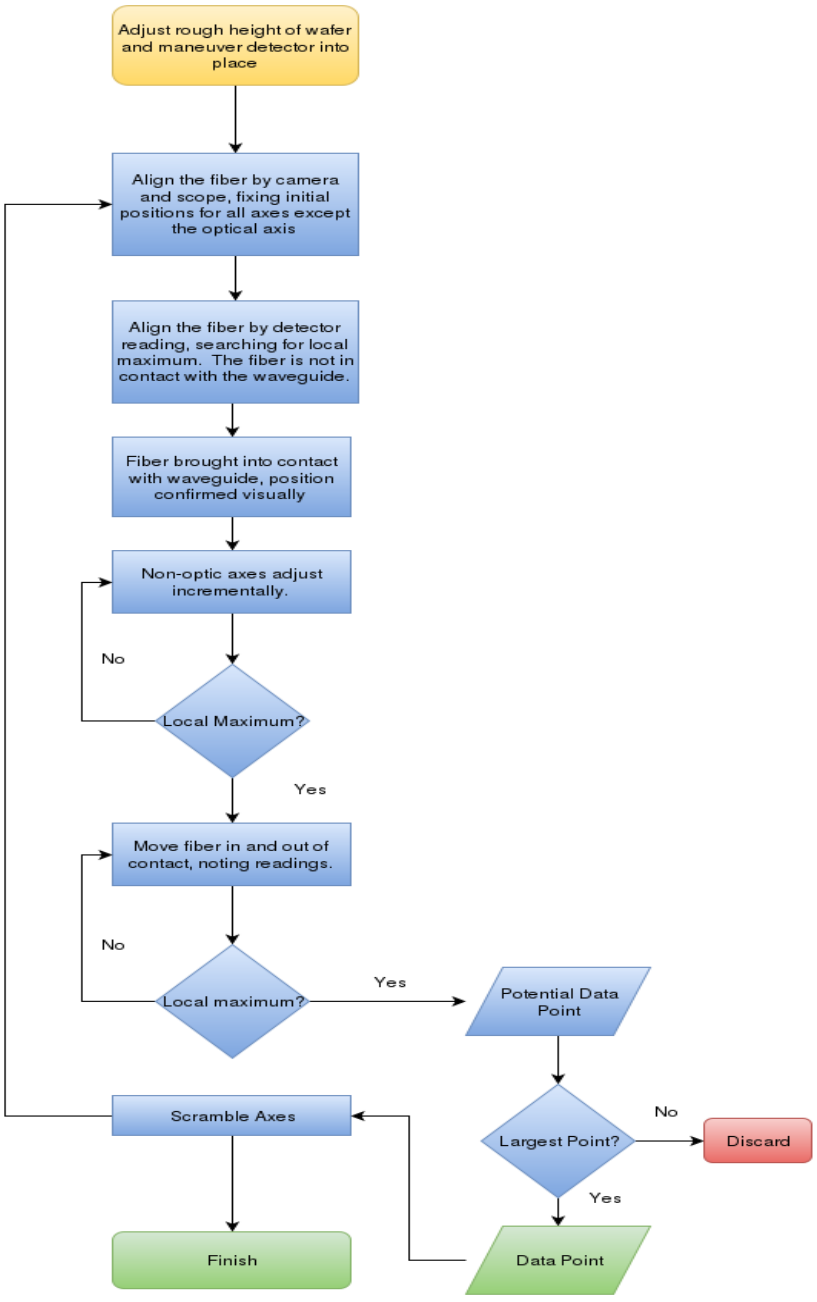

Figure 4.1 Data Collection Methodology Flowchart

The process shown in Figure 4.1 was used for the collection of all data points. Six data points were taken for each waveguide on each sample, meaning the "scramble axes" step was performed six times.

4.5 Data Processing

The basic design of the experimental apparatus is simple. It consists entirely of a HeNe laser, an objective lens for coupling into a fiber, a multi-mode fiber, the sample, a second multi-mode fiber, and a detector. The light travels from the laser and is focused onto the first multi-mode fiber (50μm core, graded index), which then carries the light to the sample. The fiber abuts the sample and delivers the light into the insertion wedge. The transmitted signal is then passed directly to a Newport 818 photodetector.

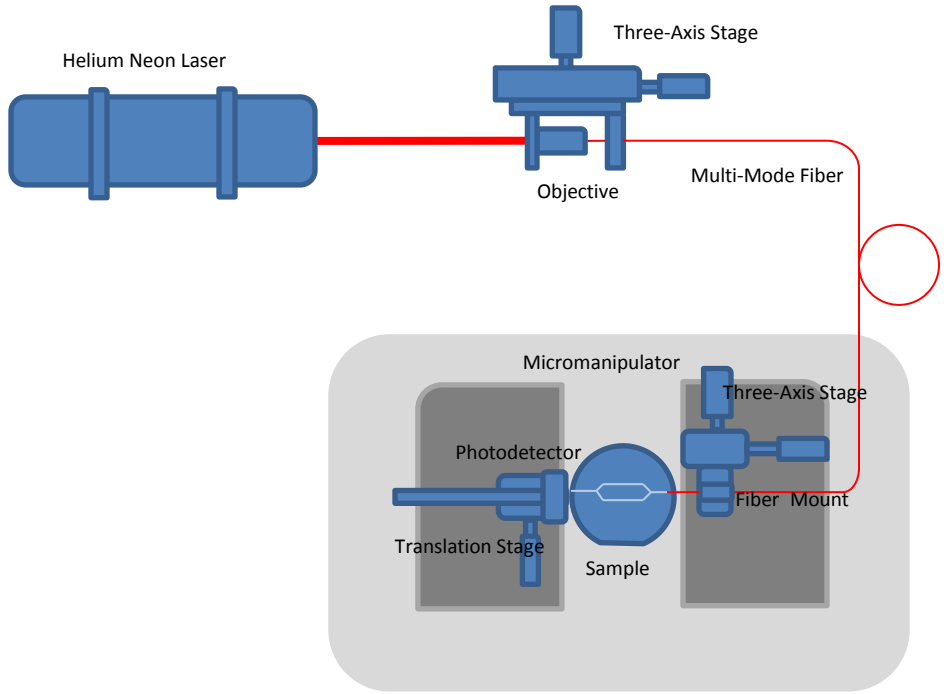

Figure 4.2: Block Diagram of Apparatus

The block diagram in Figure 4.2 shows the relative simplicity of the apparatus. Light is passed from a laser to a mounted objective, which focuses the light onto a multi-mode fiber. The

multi-mode fiber is then brought up to the sample, transferring the power by butt coupling. The light radiates freely from the sample before reaching the detector.

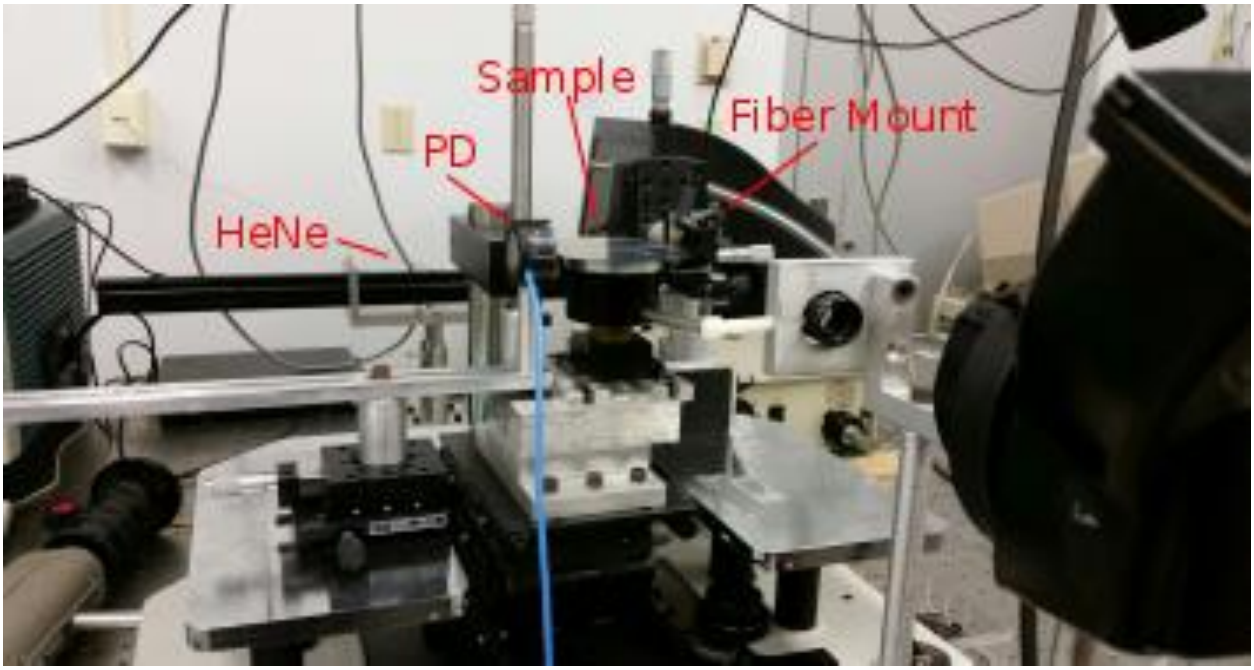

Figure 4.3 Experimental Apparatus in Use with Labeled Components

The apparatus in Figure 4.3 is visible (nearly) in full. In the back, the long black tube housing the laser can be seen. From there, the light hits the coupler (blocked in this picture), which couples the beam into the fiber. Several feet of excess fiber wind around the table just out-of-screen. The chuck on which the sample is mounted can be seen easily in the center of the shot. To the right is the fiber holder and its translation stage. The light enters the sample from this side. To the left is the photodetector, pressed closely against the sample. A great deal of mounting brackets were required to secure the sample due to the required height. The black apparatus in the foreground is an optical scope used to assist in alignment. The magnification is aided by the lens slightly in front of it. During operation, the camera visible in the lower left is mounted above the apparatus. It is not attached at this time so as to prevent possible damage to

the equipment during setup. The tall silver rod in the center of the frame holds its mounting brackets.

The apparatus is depicted in full detail in Figure 4.3. In the back, the HeNe laser is directed to an objective coupler, which focuses the light onto the tip of the fiber (not visible). The objective coupler is mounted upon a three-dimensional translation stage which allows for precise alignment with the beam. A detail view of this apparatus is shown in Figure 4.4. A fiber winds its way through to a holder, which pushes the fiber into contact with the sample. A detailed view of this is presented in Figure 4.5 and Figure 4.6. The foreground shows a small lens and scope apparatus used for aiding alignment.

The sample holder, fiber holder, and detector stage were built on a Signatone probe station. This allowed a high degree of adjustability in the relative positions of the components. The fiber holder was mounted upon one-dimensional translation stages. The sample itself was mounted upon the probe station's multi-axis platform, providing two-dimensional movement to the sample. Vertical adjustments were made by a scissor jack placed underneath the sample mountings. The sample rests upon a vacuum chuck made for the probe station. The detector is mounted upon two stacked one-dimentional translation stages. The adjustment along the optical axis is controlled by a micrometer. A pinhole aperture made of thin aluminum sheet is taped to the detector to eliminate reflections and extraneous light, ensuring that the entirety of the measured signal passed through the sample.

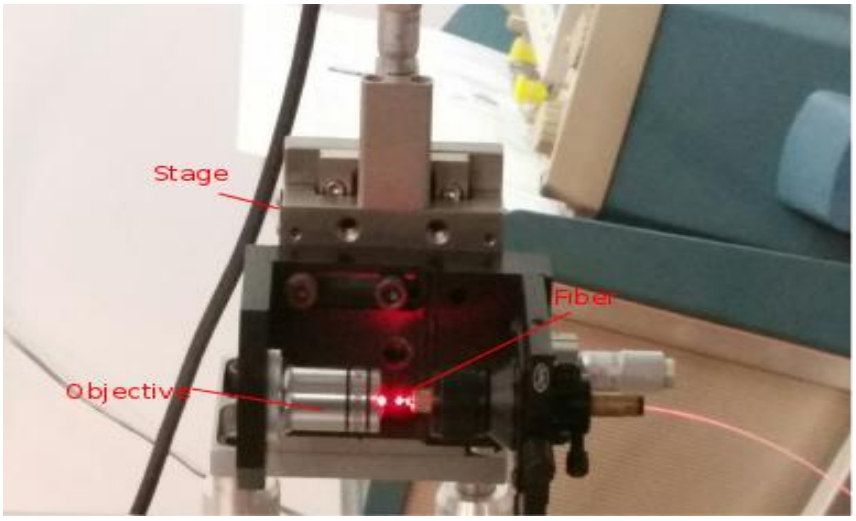

Figure 4.4 The Objective Coupler In Use With Labeled Components

The objective is mounted in a purpose-made holder, which is then supported by a 3-axis translator, shown in Figure 4.4. The objective is aligned carefully so that the laser delivers as much power as possible. The alignment was performed by using a power meter to monitor the signal coming from the fiber. The entire assembly was moved axis-by-axis until the greatest possible power reading was obtained. The fiber is brought extremely close to the objective, aligned with the aid of a photodetector as before. A bright flare of scattered light is visible on the tip of the fiber and as a reflection in the silver body of the objective. The fiber is held securely inside a brass holding tube, visible on the right of the assembly. A red tint marks the fiber where it leaves the tube. This is an example of the radiation loss discussed earlier. The fiber naturally sags under its own weight, leading to a small loss. The lens is a 40x microscope objective.

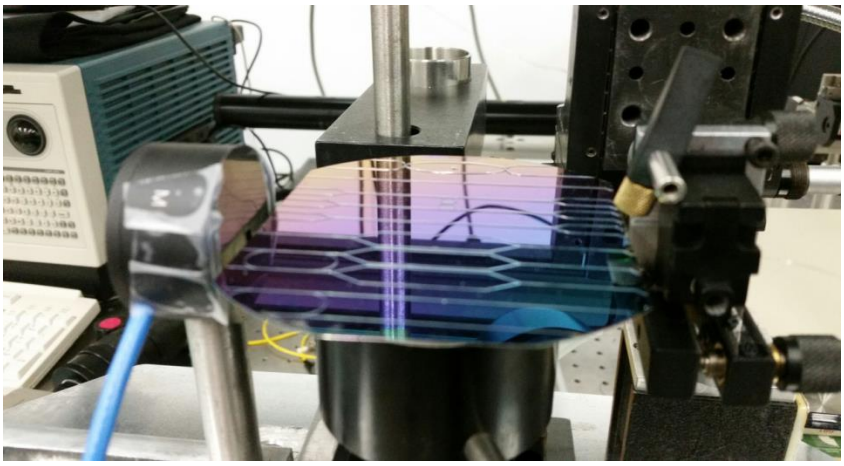

Figure 4.5 Mounted Non-Plasmonic Sample Prior to Data Collection

The mounted sample is shown in greater detail in Figure 4.5, locked in place and ready for data collection. To the left is a fiber holder, mounted in a slot and held tightly by a prism holder. This is then attached to a 3-axis translation stage that is magnetically locked to the platform. The photodetector sits to the left, mostly covered by a pinhole aperture that blocks excess light. The sample seen mounted here is the control sample, distinguished by the blue tint on the surface of the wafer from the uncovered oxide.

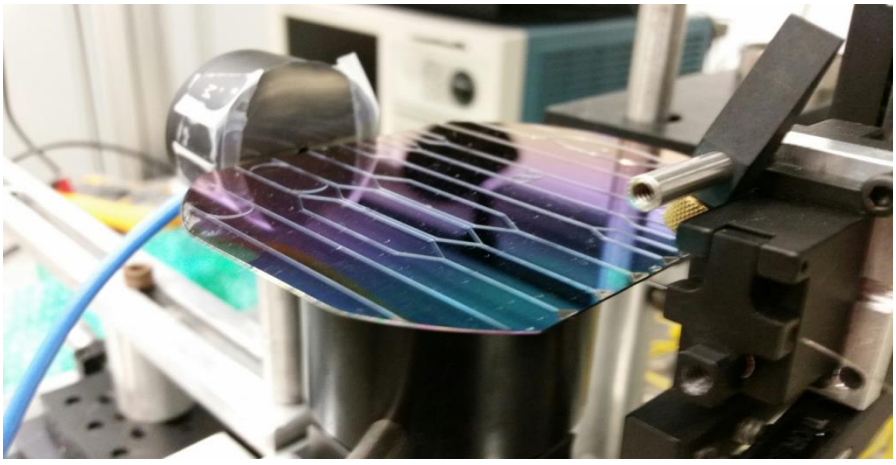

Figure 4.6 Mounted Non-Plasmonic Sample Prior to Data Collection 2

Seen in Figure 4.6 is the same sample depicted from a different angle. Unlike before, the fiber holding apparatus can be seen in high detail. The metal plate at its base provides a track on which the holder can be mounted securely. The fiber is shown in a relaxed position, kept far from the sample as to avoid potential damage. A small quantity of dust is visible on the surface of the sample. This is inevitable in any non-controlled environment and does not negatively impact data collection.

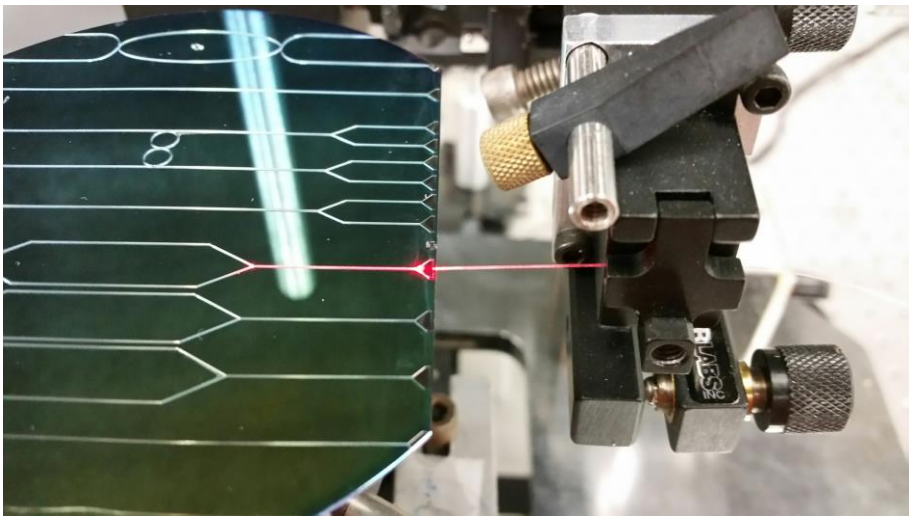

Figure 4.7 Insertion Fiber Aligned With Wedge on Non-Plasmonic Sample

Figure 4.7 depicts the apparatus in use. The fiber is set firmly against the insertion wedge and locked in place. A considerable amount of scattered light is visible emitting from both the fiber and the waveguide.

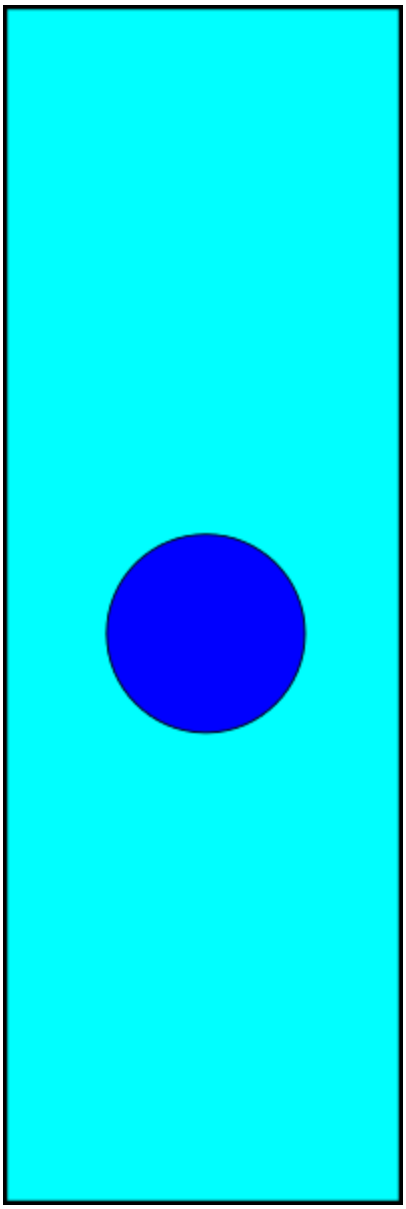

Figure 4.8 Scale Comparison of Fiber and Waveguide Cores

Figure 4.8 illustrates the size difference between the core of the fiber and waveguide. The fiber has a core diameter of 50μm, while the waveguide is a rectangle of dimension 100μm by 230μm.

5. Results and Discussion

5.1 Fabrication Results

The fabricated wafers were examined under optical (Figure 3.7) and scanning electron (Figures 5.2-5.6) microscopy. The profile of the waveguide was taken by surface profilometer and an estimate of surface roughness made. The surface profile can be seen in Figure 5.8.

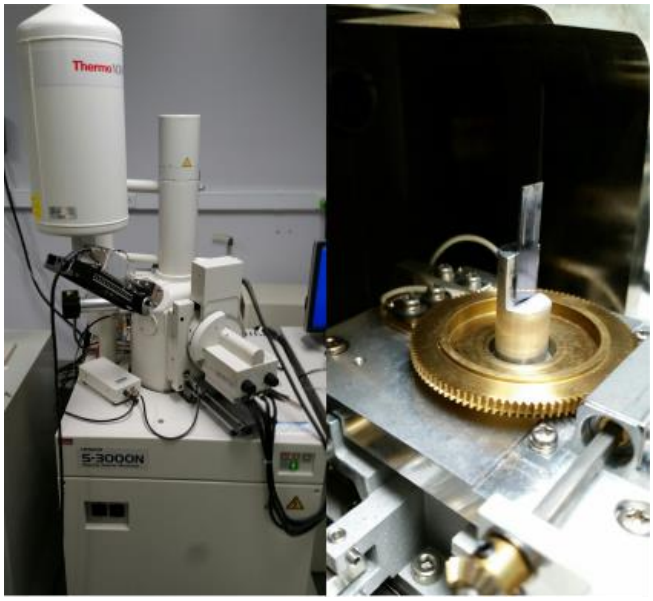

Figure 5.1 Scanning Electron Microscope and Vertically Mounted Sample in Loading Chamber

Figure 5.1 shows the Hitachi S-3000N scanning electron microscope (left) used for all SEM images herein and a mounted sample (right). A right-angle mount was used for Figure 5.5 and 5.6 to see the cross section of the wedge and waveguide. Figures 5.2 through 5.4 used a flat stage. The sample seen loaded here is a pair of insertion wedges that were part of the star coupler assembly.

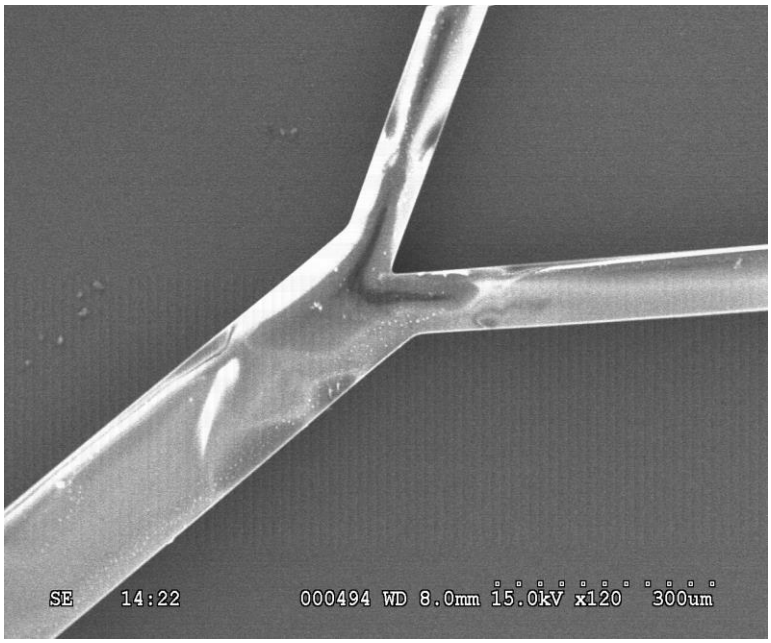

Figure 5.2 SEM Image of Mach-Zehnder Bend at 120x Magnification

Figure 5.2 is an SEM image of the opening bend of a Mach-Zehnder taken at 15.0kV and 120x magnification. The varying regions of light and dark are due to charging of the surface by incident electrons. This sample was coated with 50 nm of aluminum to reduce charging, but a great deal of the aluminum was washed away during the numerous cutting operations required to prepare the sample for viewing.

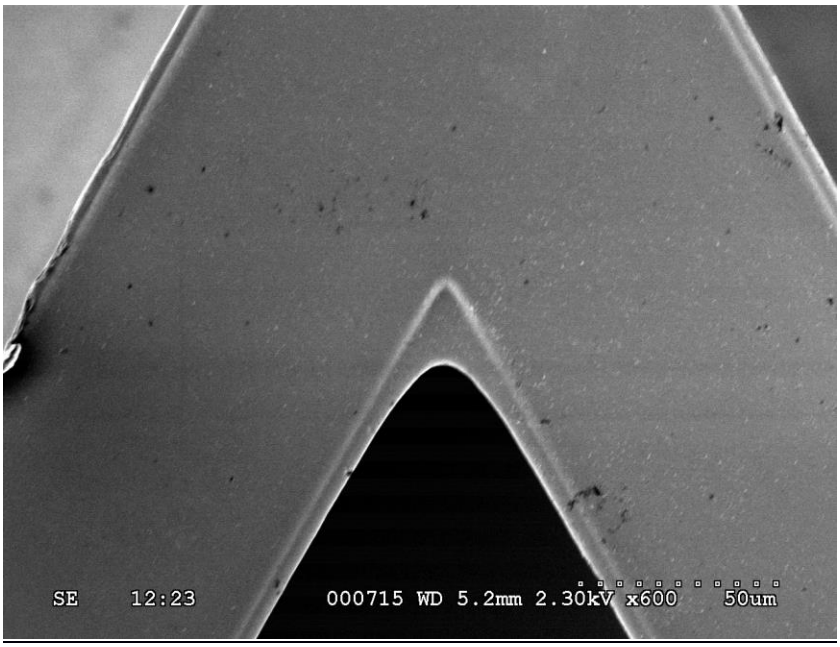

Figure 5.3 SEM Image of Mach-Zehnder Bend at 600x Magnification

Figure 5.3 shows an extreme close-up of the inside of the bend in the Mach-Zehnder arrangement taken at 2.30kV and 600x magnification. A small amount of "webbing" is visible between the arms of the device, just below the apex. This is undeveloped SU-8 protected by the geometry of the bend from exposure to the developing solution. This excess material is extremely thin relative to the height of the waveguide and is presumed to not significantly affect its performance.

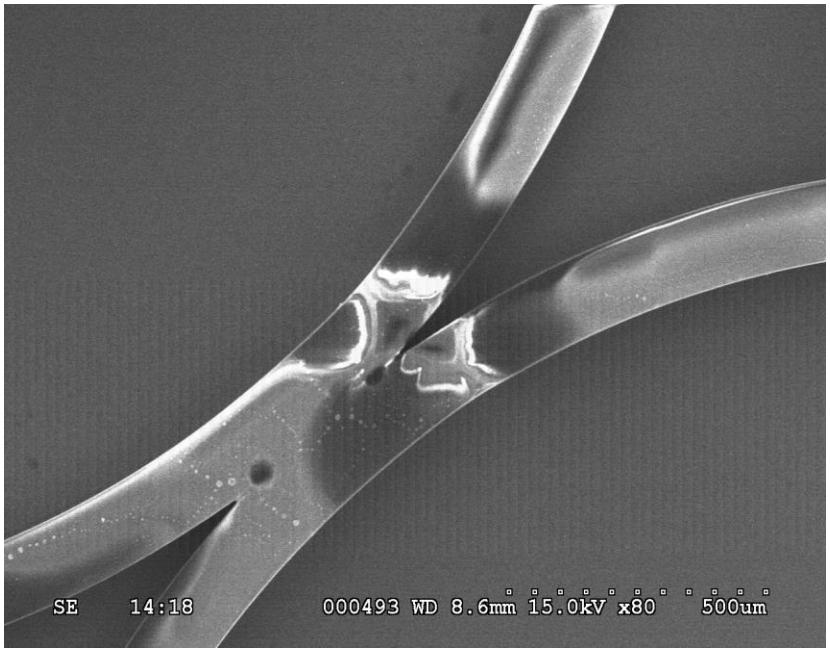

Figure 5.4 SEM Image of Ring Coupler at 80x Magnification

Figure 5.4 pictures the joint ring coupler used to connect two star couplers. Again, alternating regions of light and dark result from surface charging and are almost unavoidable at high voltages. The smoothness of the joint between the rings indicates that the junction is a single piece with no air gap.

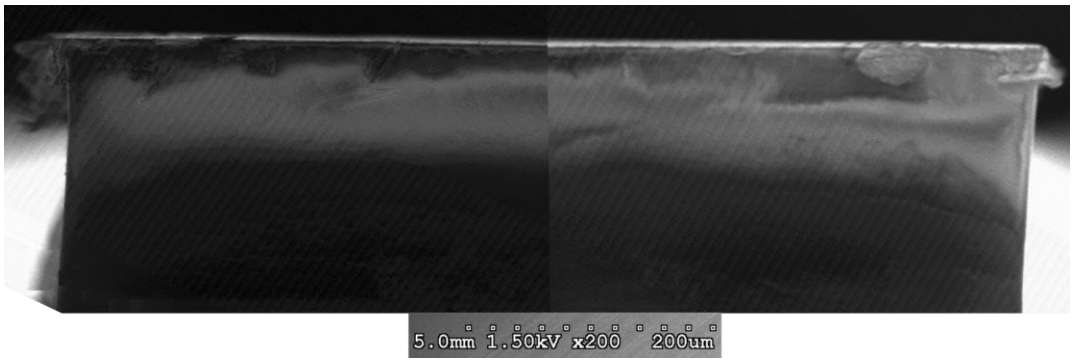

Figure 5.5 Non-Scaled Digital Reconstruction of SEM Image of Insertion Wedge at 200x Magnification

Figure 5.5 is a reconstruction of the insertion wedge, produced by cropping and blending multiple pictures to produce a single image. Note that the width is not to scale, as the extreme aspect ratio (over 10:1) would make it impossible to fit on a page. The image is also canted

slightly right due to the viewing angle used. Significant residue can be seen along the top edge of the waveguide. This is an outside contaminant, not part of the waveguide. It is likely a combination of dust and debris from sawing and transporting the sample.

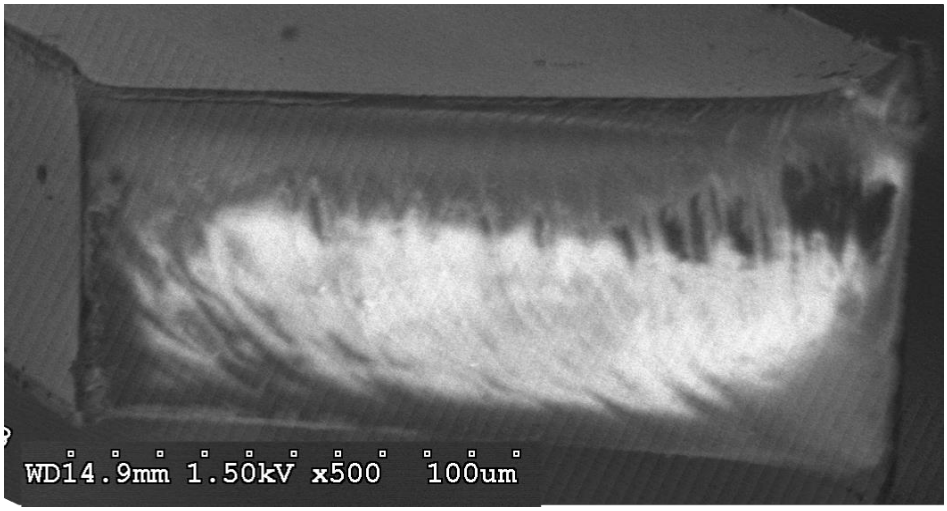

Figure 5.6 SEM Image of Waveguide Profile at 500x Magnification

Figure 5.6 depicts the profile of a waveguide, taken at 1.5kV and 500x magnification. Again, the light and dark bands are caused by charging. This waveguide was cleaved from the cut surface and mounted sideways on a right-angle mount. As such, there is no metallic coating to help reduce surface charging. The waveguide flares noticeably at its base (right). This is a result of the diffusion of photoacids during the lithography process. These flared edges extend only a few microns from the body of the waveguide and do not significantly affect its optical properties.

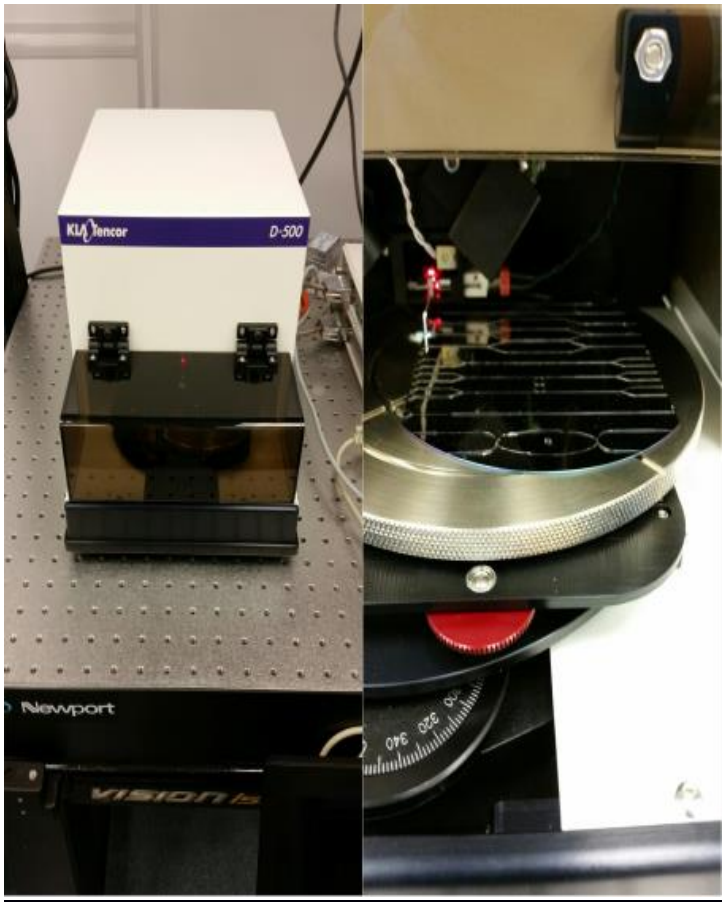

Figure 5.7 Surface Profilometer and Loaded Metal-Coated Sample

The Tencor D-500 Surface Profilometer is shown in Figure 5.7. This profilometer (left) was used to measure the average waveguide height across each sample. On the right,a nichrome coated sample is loaded into the device for measurement.

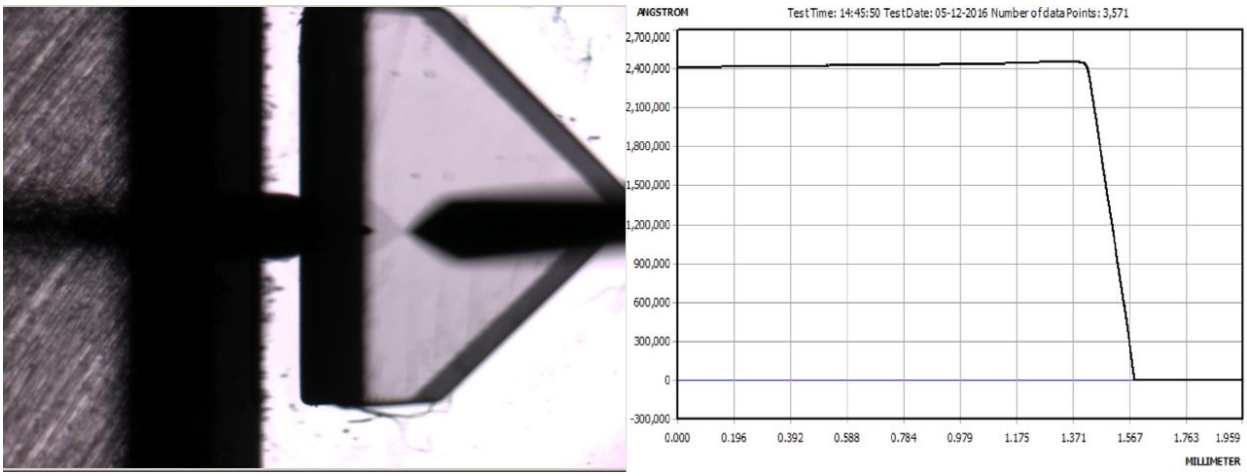

Figure 5.8 Surface Profile of Insertion Wedge on Metal-Coated Sample

Figure 5.8 shows the profilometer mid-scan (left) and the surface profile of the insertion wedge (right). The height of the waveguides made it impossible to take a full-width profile, so the tip was placed atop the waveguide and run off the edge. The profile indicates a very slanted sidewall, though SEM images do not collaborate this. It is most likely that the triangular face of the tip caught on the side of the waveguide as it dropped, making the sidewall appear much less vertical than it is. The height of this sample is 233.33um from peak to trough.

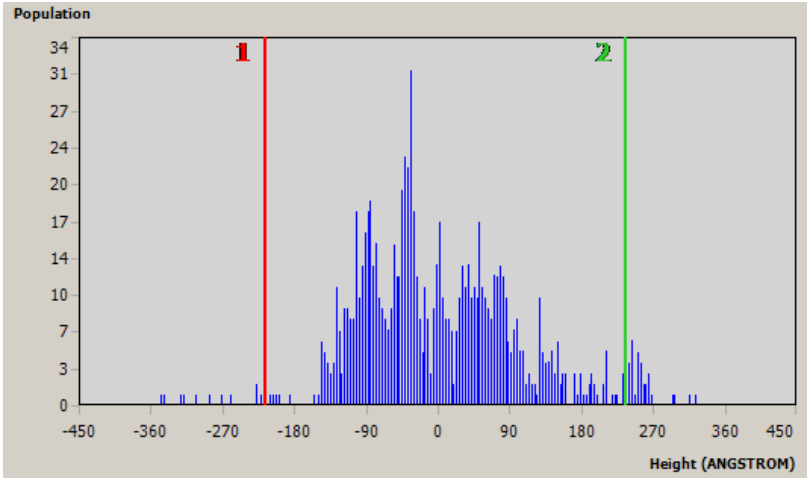

Figure 5.9 Histogram of Heights Recorded by Profilometer

Figure 5.9 shows the frequency distribution of heights. The x axis shows the deviation from zero in angstroms and the y axis the population of collected points that exhibit this height. From this data, a root-mean-square surface roughness of approximately 5.6nm was obtained. The true surface roughness is likely slightly lower. The significant envelope to the right of the distribution is likely a result of the slight cant of the waveguide surface and is not representative of the surface quality.

5.2 Ellipsometry of SU-8

An Ellipsometer was used to measure the amplitude ratio (Ψ) and phase shift (Δ) upon reflection, collectively called the Ellipsometry parameters. From these parameters, it is possible to calculate a great deal of information about the surface, including its dielectric function and complex refractive index.

Figure 5.10 Ellipsometer Measuring Optical Constants of SU-8 on Thermally Grown Silicon Dioxide

Figure 5.10 shows the Ellipsometer used to analyze the SU-8. A multiple-wavelength source on the left illuminates the sample, mounted in the center. A series of internal reflections within the sample induce a phase shift and change in amplitude of the wave. Light is collected

by the detector on the right and analyzed. The sample consists of a 100µm layer of exposed (but not hard baked) SU-8 3050 atop 533nm thermal-grown oxide. This sample closely mirrors the fabrication conditions of experimental samples.

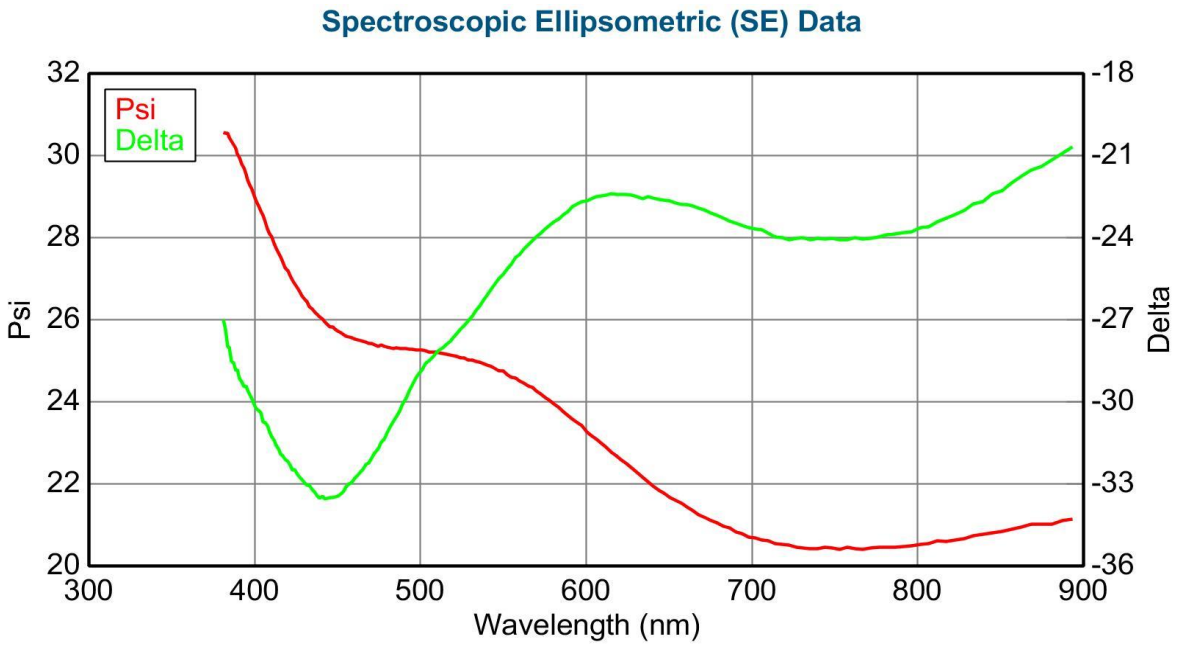

Figure 5.11 Psi/Delta Plot for Thick SU-8 on Thermally Grown Silicon

Figure 5.11 shows the Psi and Delta curves of the sample. Data was collected from 380nm to 890nm. Normally, an analytic function would be fit to the data to assist in estimating additional parameters such as the Cauchy coefficients and thickness of layers. However, since the objective is simply to calculate the dielectric function, this step is not required and was omitted.

Calculation of optical properties from Ellipsometry parameters begins with finding the complex reflectance ratio.

$$\rho = tan(\Psi)e^{i\Delta} \tag{5.1}$$

From here, it is possible to directly calculate the complex refractive index of the film,

$$\tilde{n} = \frac{\sqrt{1-4sin^2(\theta_0)\rho+2\rho+tan^2(\Psi)e^{i\Delta}}\tilde{n}_0 sin(\theta_0)}{cos(\theta_0)(1+\rho)} \quad (5.2)$$

where θ_0 is the angle of incidence and $\tilde{n}_0$ is the complex refractive index of the immersing medium (typically air). The complex index of refraction can be calculated for each wavelength by this method. From here, it is also possible to find a number of other important optical parameters like the attenuation coefficient κ

$$\tilde{n} = n(\omega) + i\kappa(\omega) \quad (5.3)$$

the dielectric function

$$\epsilon = (\tilde{n})^2 \quad (5.4)$$

which can also be written as

$$\epsilon(\omega) = \epsilon_1(\omega) + i\epsilon_2(\omega) \quad (5.5)$$

which better represents its complex nature.

With this framework established, it is simple to evaluate the index of refraction or nearly any other optical quantity at any wavelength. Table 5.1 gives the values of these optical parameters at a few select wavelengths.

Table 5.1 Ellipsometry Parameters and Derived Values

Wavelength (nm)	Ψ	Δ	n	κ	ϵ_1	ϵ_2
381.313	30.708	-25.758	1.5019	-0.1321	2.2382	-0.3968
627.556	22.620	-22.642	1.6307	-0.1960	2.6077	-0.6392
630.738	22.490	-22.719	1.6304	-0.1976	2.6191	-0.6443
633.953	22.371	-22.821	1.6327	-0.1968	2.6270	-0.6426
893.524	20.984	-21.887	1.6683	-0.1943	2.7455	-0.6483

It is immediately evident that the index of refraction given here is considerably different from the index of refraction of SU-8 given earlier. This is not unexpected, given the extremely delicate nature of such experimentation. SU-8 is not a homogeneous material, immediately making calculations from Ellipsometry difficult. Furthermore, the refractive index of SU-8 varies greatly with the fabrication process; changes in index as great as 0.05 often occur as a result of differing recipes (most notably bake duration and temperature). It is also worth noting that the SU-8 used here had passed its expiration date.

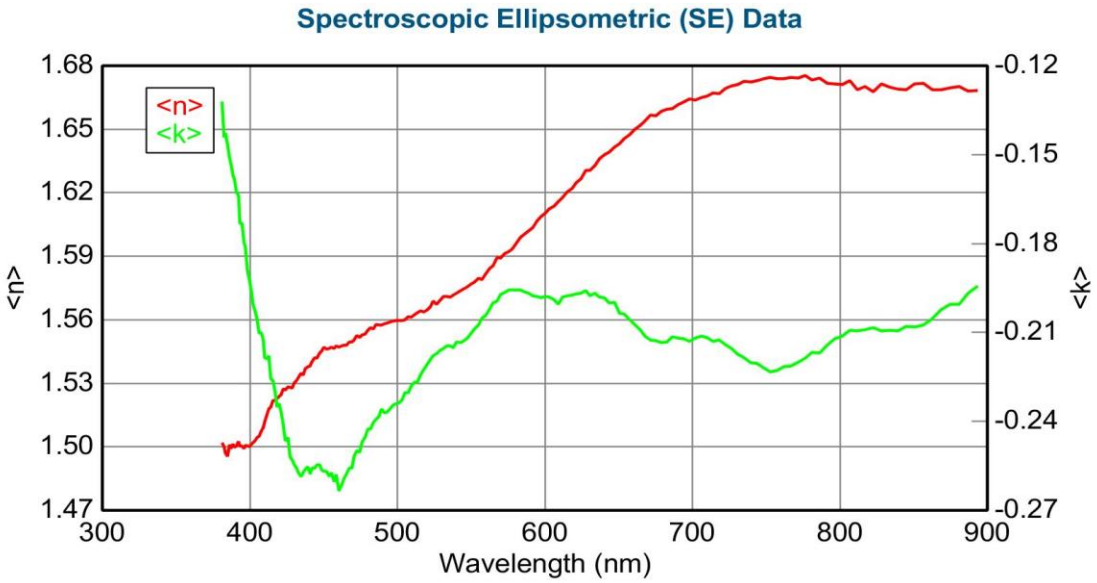

Figure 5.12 Refractive Index of SU-8 Derived From Psi/Delta Data

Figure 5.12 shows both components of the refractive index of SU-8. Both curves are significantly rougher than most such plots. This is likely due to the difficulty of performing Ellipsometry on SU-8. Calculation of optical properties from Ellipsometry parameters requires the assumption that the film is homogeneous and isometric. This is almost never the case in any resin, as chains of varying length, impurities, and differently aligned molecules often violate these assumptions.

5.3 Experimental Results

Results were obtained for samples with metal film and samples without. Data was collected for straight-line waveguides, as well as for the Mach-Zehnder orientation. Six data points were taken for the straight waveguide for both metallic and non-metallic samples. Six data points were also taken for the Mach-Zehnder on the metal-coated sample. The data points presented here are the mean of much larger data sets, presented in full in Appendix A. Twenty attempts were made to detect a signal on the non-coated Mach-Zehnder. All measurements fell below the noise threshold of the instrument. This indicates a total lack of transmission.

Table 5.2 Non-Metallic Straight Line Transmission at 633nm

Transmitted Power (μW)±0.001μW
1.094
1.074
1.077
1.086
1.090
1.088

Table 5.3 Non-Metallic Straight Line Transmission Statistical Analysis

Mean (μW)	Standard Deviation (μW)	Variance (μW)	Range (μW)
1.084	0.00708	6.017E-005	0.02

Table 5.4 Metallic Straight Line Transmission at 633nm

Transmitted Power (μW) ± 0.001μW
1.076
1.084
1.070
1.088
1.069
1.074

Table 5.5 Metallic Straight Line Transmission Statistical Analysis

Mean (μW)	Standard Deviation (μW)	Variance (μW)	Range (μW)
1.077	0.00699	5.857E-005	0.019

Table 5.6 Metallic Mach-Zehnder Transmission at 633nm

Transmitted Power (μW) ± 0.001uW
0.086
0.090
0.092
0.089
0.090
0.092

Table 5.7 Metallic Mach-Zehnder Transmission Statistics

Mean (μW)	Standard Deviation (μW)	Variance (μW)	Range (μW)
0.0898	0.00203	4.967E-006	0.006

5.3 Discussion

The data consists of two distinct sets, one comparing the loss in the straight waveguide and the other in the Mach-Zehnder waveguide. In the straight waveguide, there was no appreciable difference between the metallic and non-metallic samples. A mere 0.007uW separated the mean of the two trials. The standard deviation of both sets were comparable with this separation, indicating that it may just be a phantom of the statistics.

It is, however, entirely possible that the nichrome samples exhibited higher loss on the straight waveguide. Sefunc et al [6] reported a similar drop in transmission as a result of the addition of a metallic film. Some amount of light should always be interacting with the metal film and generating SPP. The high loss of plasmonic slab waveguides would support a drop in transmission due to this unwanted coupling. The magnitude of the difference is expected to be very small due to the limited coupling between the waveguide and the metal film. The sheer size of the waveguide means that the bulk of the power is carried far away from the nichrome film, limiting interaction.

Earlier, an estimation of loss in the waveguide predicted a loss of approximately -9.0dB from coupling and propagation. During alignment of the free-to-fiber coupler, the power being transmitted through the insertion fiber was measured as 7.928uW. This corresponds to a loss of -8.6dB through the straight waveguide, lower than anticipated. This is likely because the coupling loss estimation was intentionally high. The fiber was likely in flush contact with the waveguide, providing minimal loss.

The data from the Mach-Zehnder is a different story. There was no transmission through the non-metallic samples. This is, without a doubt, due to the extreme turn forced by the hard-angled device. The noise threshold of the detector in the room was measured to be about 0.0012 μW. In order for the signal to be unrecoverable, a total loss of at least 28.2 dB is required, over triple the loss in a straight waveguide.

In the nichrome-coated sample, a mean transmission of 0.0898 was recorded, corresponding to a total loss of -19.5dB. This number is still substantial, but still represents a significant improvement over the non-metallic samples. In addition to the effect of the split, the optical path the Mach-Zehnder was approximately 1.22mm longer, adding -0.01 extra dB of loss. This is not a significant, or even detectable loss.

As such, it can be concluded that the excess loss encountered in the Mach-Zehnder is due entirely to the y-split, which was partially counteracted by the inclusion of a nichrome film. This loss reduction is likely due to the containment of the "ripples" noted in Figure 3.6. Since no nichrome was directly underneath the waveguide, much of the propagating light was likely lost to radiation.

6. Limitations

The greatest limitation of this work is the size of the waveguides. Due to the need to be able to achieve easy and efficient butt coupling, the waveguides were designed to be extremely large. While most waveguides used in dielectric-to-metal coupling use waveguides on the order of the wavelength of light used, these waveguides were 100x230μm in profile and over 8cm long.

As a result, the coupling to SPP was poor, leading to a much higher bending loss in the experimental sample than could have been achieved, had the waveguides been significantly smaller. The results obtained would also have been much more applicable in current photonic devices. It is extremely uncommon for surface-mounted waveguides to be on the order of 100μm.

Another limitation of this work is the poor coupling caused by an inefficient coupling regime. Plasmonic surface-mount waveguides have demonstrated their ability to confine light, but side-by-side coupling is not a particularly efficient regime. This is compounded by the aforementioned limitation of size. The coupling paradigm used is not nearly as efficient as expected due to poor concentration of power near the metal surface.

The result of these limitations is an overall unsuitability to practical application. While the concept of coupling to nichrome slab waveguides for bending-loss prevention was successfully demonstrated, vastly more efficient designs have already been produced. The

enormous losses encountered during experimentation are not conducive to the construction of an efficient, useful optical device.

7. Conclusions and Future Work

7.1 Conclusions

A fabrication process for the production of SU-8 slab waveguides was created. A mask was designed to shape waveguides by photolithography. Straight line, star coupler, Mach-Zehnder, U-bend, and linkage waveguides were created using a one-mask process. Multiple samples were fabricated, both with the waveguides laying atop bare field of silicon dioxide and also with a nichrome thin film surrounding the waveguides.

An experimental apparatus was constructed to allow comparison of the sample. Light of 633nm was coupled into the waveguides and the output power recorded. Data was collected for both metallic and non-metallic samples for the straight line waveguide and for the Mach-Zehnder waveguide.

Little-to-no difference was observed between the metallic and non-metallic straight line waveguides. This result is supported by theory and a review of existing literature. The presence of nichrome film had a considerable impact on transmission through the Mach-Zehnder. Extreme bend angles attenuated the signal within the control sample, while power was successfully transmitted through the nichrome-clad sample, albeit at high loss. As such, a reduction of bending loss through the use of slab-to-slab coupling between a dielectric and metal waveguide was demonstrated.

Experimental error should be limited by the iterative data-taking process, but several outstanding sources of error likely still exist. Some variance between data points almost assuredly arises from subtle differences in coupling conditions. Truly perfect alignment requires subwavelength precision. Misalignments are likely on the micrometer scale. When aligning optical fibers, even the ambient air currents can create a measurable variation in measured power.

It is also possible that the fiber end suffered damage throughout the data collection process. While great care was taken to protect the fiber, any contact between the fiber and waveguide may result in a scratch on either. Scratches in the waveguide are unlikely to meaningfully affect the results due to the relative size of the waveguide, but any damage to the core of the insertion fiber will result in increased scattering loss at the damaged surface.

Variations in measured power may also arise from variations in input power. No laser emits a truly constant output. Fluctuations are normal and were observed during testing. These fluctuations in measured power made data collecting significantly more time consuming than it would otherwise have been and almost assuredly resulted in errors greater than the uncertainty. It is likely that this is the single greatest source of error, as compensating for it is relatively difficult.

The experimental data was supported by a model of electric field distributions within a like-dimensioned waveguide (Appendix B). The study provides a direct comparison same-index propagating modes in waveguides with and without metal. When metal was present, the electric

field intensity is greatly increased on the sides of the waveguide and on the substrate. This result suggests both successful coupling to the plasmonic film and a fundamental change in the distribution of modes. The increased field intensity along the inside wall of a bend could significantly improve the transmission of the curve by reducing dispersion from bending and minimizing radiative losses.

7.2 Future Work

The most productive avenue for future work would be to address the primary limitation of this research, the size of the waveguides. As of yet, no published studies utilize nichrome films in this application, opting instead for gold or silver in almost every instance. It is the belief of the author that the use of nichrome films holds some promise in such applications as a result of its strong oxidation resistance and excellent adherence to both silicon and silicon dioxide. Additionally, few experimental studies have been performed to demonstrate slab-to-slab coupling between dielectrics and metal films. The majority of plasmonic waveguide research has been directed towards slot-to-slot systems.

Future work could also include the use of different metals in a similar construction. Extremely few studies utilize waveguides of the size constructed here. As such, there is no data available for plasmonic confinement in multi-mode waveguides using any metal other than nichrome. It is expected that the use of either gold or silver would significantly reduce loss in hard-angle bends due to their relatively long plasmon propagation length.

List of References

[1] Yang, R., et al. “Efficient light coupling between dielectric slot waveguide and plasmonic slot waveguide.” *Optics Letters* 35.5 (2010) 649-651.

[2] Veronis, G., et al. “Modeling of Plasmonic Waveguide Components and Networks.” *Journal of Computation and Theoretical Nanoscience* 6 (2009) 1808-1826.

[3] Krasavin, A. V. and Anatoly V. Zayats “Silicon-based plasmonic waveguides.” *Optics Express* 18.11 (2010) 11791-11799.

[4] Sefunc, M. S., et al., M Pollnau, and S M Garcia-Blanco “Low-loss sharp bends in polymer waveguides enabled by the introduction of a thin metal layer.” *Optics Express* 21.24 (2013) 29808-29817.

[5] Saleh, B. E. A. and M. C. Teich *Fundamentals of Photonics.* Second Edition. Hoboken: John Wiley & Sons, 2007.

[6] Taylor, H. F. and A. Yariv “Guided Wave Optics.” *Proceedings of the IEEE* 62.8 (1974) 1044-1060.

[7] Palais, J. C., *Fiber Optic Communications*. Fourth Edition. Upper Saddle River: Prentice Hall, 1984

[8] Hunsperger, R.G., *Integrated Optics Theory and Technology*. Fifth edition. Berlin: Springer, 2002.

[9] Sambles, J. R., G. W. Bradbery, and F. Yang “Optical excitation of surface plasmons: an introduction.” *Contemporary Physics* 32.3 (1991) 173-183.

[10] Kayaku Microchem “SU-8 3000 Permanent Epoxy Negative Photo Resist.” Data Sheet.

[11] Parida, O. P. and N. Baht “Characterization of Optical Properties of SU-8 and Fabrication of Optical Components.” *International Conference on Optics and Photonics* 2009.

[12] Prajzler, V., et al. “Flexible Polymer Planar Optical Waveguides.” *RadioEngineering* 23.3 (2014) 776-782.

[13] Microchem “SU-8 Permanent Photoresists.” Datasheet.

[14] Kern, W., *Handbook of Semiconductor Cleaning Technology*. Park Ridge: Noyes Publishing, 1993.

Appendices

Appendix A

Appendix A gives the unabridged versions of the data sets presented in Tables 5.2, 5.4, and 5.6. Each value presented in those tables is the highest value of each data collection. Herein lies every value recorded for each of these sets. The first value of each set in these tables is the highest value, the one reported in Chapter 5.

Table A.1 Unabridged Non-Metallic Straight Line Transmission at 633nm.

Set 1	Set 2	Set 3	Set 4	Set 5	Set 6
Power (μW)	Power (μW)	Power (μW)	Power (μW)	Power (μW)	Power (μW)
1.094	1.074	1.077	1.086	1.090	1.088
1.092	1.074	1.076	1.080	1.089	1.088
1.090	1.071	1.073	1.085	1.088	1.083
1.094	1.072	1.077	1.083	1.082	1.085
1.091	1.070	1.073	1.084	1.089	1.084
1.090	1.073	1.076	1.083	1.088	1.084
1.093	1.068	1.072	1.084	1.085	1.081
1.088	1.071	1.073	1.079	1.083	1.083
1.090	1.068	1.075	1.084	1.088	1.086
1.083	1.066	1.074	1.085	1.083	1.084

Table A.2 Unabridged Metallic Straight Line Transmission at 633nm

Set 1	Set 2	Set 3	Set 4	Set 5	Set 6
Power (μW)	Power (μW)	Power (μW)	Power (μW)	Power (μW)	Power (μW)
1.076	1.084	1.070	1.088	1.069	1.074
1.069	1.080	1.060	1.083	1.065	1.072
1.066	1.083	1.067	1.081	1.066	1.069
1.069	1.082	1.064	1.082	1.062	1.071
1.075	1.081	1.069	1.075	1.062	1.067
1.072	1.076	1.070	1.085	1.066	1.074
1.068	1.080	1.064	1.082	1.066	1.070
1.076	1.084	1.063	1.086	1.063	1.073
1.073	1.078	1.062	1.084	1.061	1.066
1.069	1.077	1.070	1.088	1.067	1.070

Table A.3 Unabridged Metallic Mach-Zehnder Transmission at 633nm

Set 1	Set 2	Set 3	Set 4	Set 5	Set 6
Power (μW)	Power (μW)	Power (μW)	Power (μW)	Power (μW)	Power (μW)
0.086	0.090	0.092	0.089	0.090	0.092
0.079	0.088	0.090	0.088	0.090	0.084
0.084	0.083	0.092	0.085	0.088	0.090
0.081	0.084	0.085	0.087	0.084	0.091
0.085	0.085	0.086	0.082	0.089	0.088
0.081	0.084	0.091	0.084	0.087	0.088
0.084	0.088	0.089	0.083	0.090	0.090
0.082	0.084	0.086	0.083	0.085	0.087
0.085	0.087	0.085	0.085	0.090	0.089
0.084	0.087	0.091	0.084	0.085	0.091

Appendix B

Appendix B contains the results of an FDFD model constructed in COMSOL to simulate the TE mode distribution within the modeled waveguides at various wave vectors (reported here as effective refractive index). The model was simply a qualitative aid to help understand what happens within a multi-mode waveguide when a metallic film is added. The modeled waveguides exactly mirror the scale and construction of the waveguides tested in Chapter 5. Note that this model is a 2-D profile of a straight waveguide, immersed in air and seated upon a thick silicon dioxide layer. In all images, the non-metallic sample is presented on the left and the metallic sample on the right. The color represents the electric field of the TE mode, where red is positive, blue negative, and green zero.

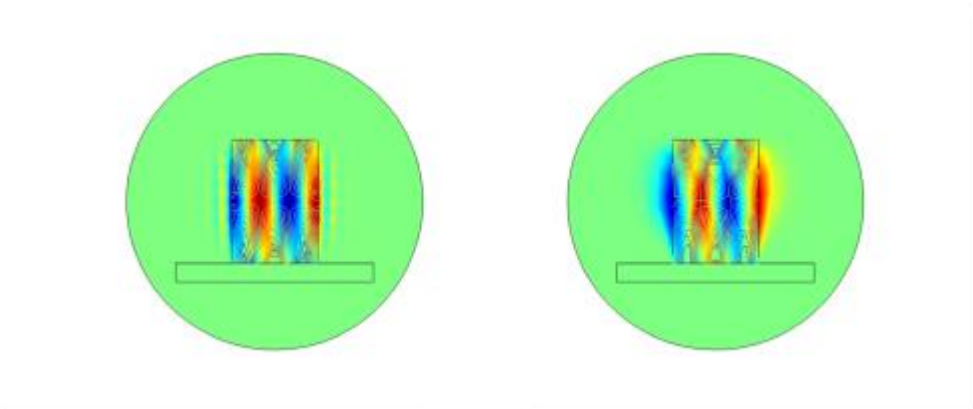

Figure A.1 n=1.59494

Figure A.2 n=1.594931

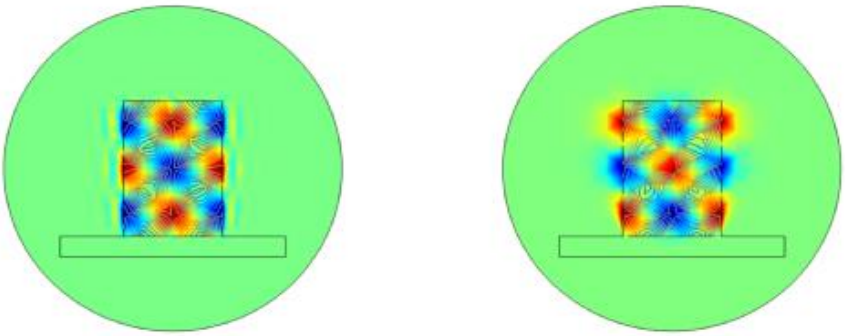

Figure A.3 n=1.594947